Additive Manufacturing 47 (2021) 102300

Contents lists available at ScienceDirect

Additive Manufacturing

journal homepage: www.elsevier.com/locate/addma

Research Paper

A rigorous test and improvement of the Eagar-Tsai model for melt pool characteristics in laser powder bed fusion additive manufacturing

P. Honarmandi [a,*], R. Seede [a], L. Xue [a], D. Shoukr [b], P. Morcos [a], B. Zhang [b], C. Zhang [b], A. Elwany [b], I. Karaman [a], R. Arroyave [a,b,c]

[a] *Department of Materials Science and Engineering, Texas A&M University, College Station, TX, USA*
[b] *Department of Industrial and Systems Engineering, Texas A&M University, College Station, TX, USA*
[c] *Department of Mechanical Engineering, Texas A&M University, College Station, TX, USA*

A R T I C L E I N F O

Keywords:
Additive manufacturing
Bayesian inference
Markov Chain Monte Carlo
Uncertainty quantification
Uncertainty propagation

A B S T R A C T

The accurate prediction of the thermal histories and melt pool characteristics during additive manufacturing (AM) is necessary to understand the factors responsible for the quality and integrity of the manufactured part. More importantly, the determination of optimal process windows and even feed-forward and in-line feedback control of the manufacturing process require computationally cheap, fast-acting, quantitative models connecting (local) processing parameters to melt and solidification conditions. Initially developed in the context of welding, the Eagar-Tsai (E-T) model stands out among the most widely used computationally cheap models to predict melt pool characteristics during AM. Despite its widespread use, its statistical validity *in the context of AM* has yet to be thoroughly verified. In this work, we study the E-T model in a systematic manner, from an uncertainty quantification/propagation (UQ/UP) perspective. E-T model parameters are calibrated against high quality single-track experimental data on the melt pool geometries of several materials through Markov Chain Monte Carlo (MCMC) sampling. Posterior distributions of the model parameter values are then propagated. We find that there are considerable discrepancies between predicted and measured melt pool depths when process conditions correspond to keyholing. We then apply a physics-based correction and find that it is possible to achieve much better agreement with experiments without increasing significantly the complexity of the E-T model. Although there might be some uncertainties due to the missing physics and assumptions in the model, the model accuracy and trend are satisfactory for the purpose of accelerated product design under uncertainty.

1. Introduction

Metal AM has been developing at a very fast rate over recent decades [1–3]. Despite the promise of AM, significant challenges remain due to the strong connection between processing conditions and the onset of microstructural features or defects that compromise the integrity of the manufactured part. In principle, computational models connecting processing parameters to solidification conditions may provide the means to interpret experimental observations or may be used to guide the systematic exploration of the AM process space. The (local) thermal histories arising during the printing process are ultimately responsible for the microstructure, defects and properties of the final product [4,5]. Therefore, models capable of predicting the effect of process conditions on the thermal histories and melt pool characteristics should be key elements in any effort to establish quantitative process-structure-property-performance (PSPP) relationships in AM.

The simulation of thermal histories during AM is carried out by either numerical or analytical solutions, at varying levels of complexity, fidelity and, crucially, computational cost. The complex, coupled nature of the many different mechanisms prevalent during AM has motivated the development of high-fidelity numerical solutions—i.e., finite difference (FD) [5], finite volume (FV) [6–8], and finite element (FE) methods [9–12–15–18–21,22]. However, the high computational cost of these models makes their parameter calibration very difficult [4], and also hinders their application in AM process design [23,24] as their cost makes them impractical for the wide exploration of the process

* Correspondence to: Texas A&M University, Department of Materials Science and Engineering, 3003 TAMU, College Station, TX 77843–3003, USA.
E-mail addresses: hona107@tamu.edu (P. Honarmandi), rseede@tamu.edu (R. Seede), leixue11@tamu.edu (L. Xue), davidshoukr@tamu.edu (D. Shoukr), peter.morcos@tamu.edu (P. Morcos), zb19911212@tamu.edu (B. Zhang), chenzhang@tamu.edu (C. Zhang), elwany@tamu.edu (A. Elwany), ikaraman@tamu.edu (I. Karaman), rarroyave@tamu.edu (R. Arroyave).

https://doi.org/10.1016/j.addma.2021.102300
Received 20 May 2021; Received in revised form 7 August 2021; Accepted 7 September 2021
Available online 10 September 2021

parameter space. In the latter context, fast, analytical (or numerical) models with acceptable degree of fidelity vis-à-vis experiments are highly desirable.

One of the earliest approaches to the prediction of thermal histories of materials subject to the localized deposition of energy was carried out by Rosenthal [25]. Rosenthal's theory described the solution (i.e., $T(x,y,z,t)$) to the motion of a point heat source across a semi-infinite plate under conduction heat transfer [25]. This model was originally proposed for fusion welding, but later on, it received some attention from the AM community [26]. To resolve the issues related to singularities in the temperature field arising from the point heat source approximation, Eagar and Tsai [27] instead considered a moving Gaussian-distributed heat source. Despite more enriched and sophisticated recently proposed analytical models, particularly by Steuben *et al.* [4] and Schwalbach *et al.* [26], the E-T model remains popular among the metal AM community due to its simplicity and ease of deployment. A subset of these authors have used the E-T model, for example, to assess the printability of alloys subject to laser powder bed fusion (L-PBF) AM [23,24]. We must point out, however, that despite its widespread use, the E-T model has yet to be rigorously assessed in the context of AM—physical phenomena during AM are different from those occurring during welding.

The present work attempts to address this matter through the full characterization of the E-T model through the use of Bayesian parameter optimization (i.e., UQ) to estimate the most plausible values for the model parameters, given the ground truth data, accounting for the associated uncertainties. The latter may arise from lack of sufficient information, incomplete physics, inaccurate simplifications and assumptions in the model structure, as well as natural and human errors in the execution and analysis of the experiments used to calibrate the model(s) [28–31–34,35,36].

UQ is considered as one of the main elements of the simulation-assisted materials design in the integrated computational materials engineering (ICME) [37] since it can provide (i) rigorous statistically-valid metrics for the validation and verification of models/theories; (ii) statistical confidence bounds for decision support in robust- and reliability-based design [38]. UQ studies have slowly permeated the AM literature, but much work remains to be done [39]. Lopez *et al.* [40] proposed a UQ approach for L-PBF models by the identification and overall estimation of different sources of uncertainty, including uncertainties associated with numerical solutions, model parameters/input controls, and experimental data. For the second-mentioned uncertainty source, a numerical Monte Carlo (MC) technique was utilized to propagate uncertainty from the pre-assigned normally distributed input controls and parameters to the model output—i.e., melt pool width [40].

It should be noted that replacing AM models by inexpensive surrogate models, particularly Gaussian process (GP) and Polynomial Chaos Expansion (PCE), has been attracting attention in the UQ field over recent years. Kamath [41] and Hu and Mahadevan [39] quantified uncertainties by training a GP surrogate model over the E-T model and the Large-scale Atomic/Molecular Massively Parallel Simulator (LAMMPS) responses at input controls and parameters sampled through design of experiment (DOE) methods, respectively. The former work [41] directly reports the distance-based uncertainties obtained from the GP model while the latter [39] uses the surrogate model inexpensive predictions in an MC-based scheme to estimate the uncertainty of the model response. Nath et al. [42] implemented a chain of multi-level models—connecting a GP surrogate model trained over an expensive FE melting model—to a cellular automata (CA) solidification model in order to propagate the uncertainties from the material properties to microstructure to quantities of interest (QoIs). In that work, the parameters associated with the temperature-dependent material properties in the melting model, as well as the parameters related to the microstructural grain growth rate in the solidification model were defined as Gaussian distributions, which can be updated by newly acquired experimental data using a Bayesian approach [42]. Tapia et al. [43] applied a general PCE method to propagate uncertainties from the input controls of two thermal history models—analytical E-T and numerical FE thermal models—for the L-PBF processes to one of their outputs—i.e., melt pool width. This approach was benchmarked against brute-force MC simulations as well as experimental data [43].

There is also a more sophisticated surrogate-based UQ in the recent AM literature, known as the Kennedy and O'Hagan's approach. This approach takes different sources of uncertainty into account by establishing a linear relationship between data and model response whose intercept consists of the model discrepancy due to model incompleteness and the data error. While the data error is a normally distributed function, two GP surrogates are built over the model and its discrepancy and then statistically correlated and combined together for the subsequent UQ through a Bayesian sampling technique, such as MCMC [44]. It is worth noting that physical models can directly be used in this approach, provided they are not expensive [45]. This UQ method was applied by Wang et al. [46] along a chain of expensive multi-level AM models. Later, Mahmoudi et al. [47] and Seede et al. [24] employed this approach for the probabilistic calibration of the model parameters in an FE and the E-T thermal models for different AM processes, respectively. In the case of multi-level modeling, Bayesian network (BN) techniques have recently been utilized to demonstrate the statistical conditional dependencies of input and output variables along the hierarchical models through a directed acyclic graph. In this network, expensive models can be replaced by their corresponding surrogate models. BNs can address the challenge of dealing with the analysis of heterogeneous uncertainties in the probabilistic calibration of multi-level models when the models' outputs contain unobservable variables besides observable ones [39,48]. For example, Mahmoudi et al. [48] utilized a BN framework to quantify uncertainties for the parameters and multi-level output variables in a chain of models where the GP surrogate of an FE thermal model is connected to its counterpart for a phase-field simulation through an unobservable variable [48].

Despite the focus of the AM literature on the GP-based UQ that is inevitable for the expensive numerical models in the AM processes, this surrogate modeling approach—similar to other machine learning techniques—typically delivers poor predictions beyond the training data. Therefore, numerical UQ approaches, e.g., MCMC sampling methods, can be applied for more accurate predictions in the case of inexpensive analytical models. In the present work, an MCMC approach is used to statistically calibrate and validate one of the most important analytical thermal history models used by the AM community—i.e., the E-T model. For this purpose, clean, extensive data for the melt pool dimensions of single-track prints at different L-PBF process conditions are experimentally obtained for different material systems. The first batch of calibrations shows the inability of the thermal model in the prediction of melt pool depth at process conditions corresponding to the keyholing phenomenon. For this reason, another batch of calibrations is performed by taking into account a physical correction for the keyholing process conditions. It is our hope that this work provides insight into the applicability of this inexpensive analytical model in the analysis and design of AM processes.

2. Eagar-Tsai thermal model description

The E-T model is an inexpensive analytical thermal model proposed in the early '80 s to describe the thermal profile of a melt pool (and the material surrounding it) formed during fusion welding. With the significant growth in AM research, the community adopted this model as a fast, easily deployable, physically-motivated approximation to the thermal histories and melt pool characteristics of AM (particularly L-PBF) processes. The model provides a solution for the steady-state heat conduction equation where a Gaussian-distributed heat source moves across a semi-infinite flat plate with a constant speed in the x-direction. The generalized solution for this problem is expressed in the form of

Green's function that is used in a double integral over the surface of interest to obtain the temperature profile across the plate.

A more simplified solution can be obtained for the Gaussian-distributed heat source that results in a single integration over time along the moving direction. In this case, a set of discrete heat sources is considered along the moving direction, and then the rise of temperature from the initial temperature T_0 at any point of interest across the plate is calculated for many short time intervals, $[t', t' + dt')$, from the initial time 0 to final time t. The summation of all these temperature increases determines the ultimate temperature at any specific point of interest after the duration t, which can be expressed in the following integral form (for more information and mathematical derivations, see [27]),

$$T - T_0 = \frac{1}{2}\int_{t'=0}^{t'=t} dT_{t'} = \frac{q}{\pi\rho C_p\sqrt{4\pi\alpha}}\int_{t'=0}^{t'=t}\left[\frac{(t-t')^{-\frac{1}{2}}}{2\alpha(t-t')+\sigma^2}e^{\left[-\frac{(x-vt')^2+y^2}{4\alpha(t-t')+2\sigma^2}-\frac{z^2}{4\alpha(t-t')}\right]}\right]dt', \tag{1}$$

The above integration is performed through a numerical quadrature method to find the temperature profile across the plate at any given time during the thermal process. In this equation, (x, y, z) is the coordinate of the spatial point of interest where the temperature T is predicted. There are two different types of model variables associated with the heat source and material properties. From the first category, q is the absorbed (input) energy to the material per time unit, which is a fraction of heat source input power—i.e., μP, where μ is efficiency—due to the inevitable energy dissipation during AM processes resulting from different mechanisms, such as evaporation, reflection, spattering, etc. Moreover, v is the heat source velocity and, σ is the standard deviation of the Gaussian heat source. From the second category, ρ, C_p, and α are the density, specific heat capacity, thermal diffusivity of the given material, respectively. It is worth noting that the thermal diffusivity is proportional to the thermal conductivity, as $\alpha = \kappa/\rho C_p$. C_p and α/κ are considered to be two effective parameters that are temperature-independent. At the end, the integrated solution for the temperature profile can identify the locations with the temperature greater than the material melting temperature that results in the determination of melt pool dimensions—i.e., melt pool length, width, and depth—as other model outputs. This model is used to predict the melt pool dimensions of single-track prints corresponding to the given experimental conditions for laser powers and velocities.

3. Experimental procedure

Gas atomized AF9628 [24], 80Ni-20Cu, 96.8Ni-3.2 Nb, and 51.2Ni-48.8Ti powder provided by Nanoval GmbH & Co. KG are used to manufacture the L-PBF specimens. Single tracks are printed using a 3D Systems ProX DMP 200 Laser Type (fiber laser with a Gaussian profile $\lambda = 1070$ nm, and beam size $d = 80$ μm). The tracks are printed on base plates with the same composition as each of the respective alloys. Each substrate is subjected to surface grinding in order to ensure a flat and parallel surface with respect to the machine's base plate. The 51.2Ni-48.8Ti substrate is additionally sand-blasted to improve powder coverage. These tracks are 10 mm in length with 1 mm spacing between tracks. Parameters are selected based on the optimization framework developed by Seede et al. [24]. The layer thickness used for each alloy is selected using the $D80$ of the received powder, where $D_x x$ is the cumulative distribution of the powder at XX percent. AF9628, 80Ni-20Cu, 96.8Ni-3.2 Nb, and 51.2Ni-48.8Ti are printed using a powder layer thickness of 37, 53, 30, and 30 μm, respectively. Three cross sections of the single tracks are wire-cut using wire electrical discharge machining (EDM), and these specimens are polished down to 0.25 μm with water-based diamond suspension polishing solutions. A 4% Nital solution (4 mL HNO3 and 96 mL ethyl alcohol) is used to etch AF9628 single tracks, Kalling's Solution No. 2 (5 g CuCl2, 100 mL HCl, and 100 mL ethanol) is used to etch the 80Ni-20Cu and 96.8Ni-3.2 Nb single tracks, and a HF etchant (1 part HF, 3 parts HNO3, and 10 parts of DI water) is used to etch the 51.2Ni-48.8Ti single tracks to obtain cross-sectional optical micrographs. Optical microscopy (OM) is carried out using a Keyence VH-X digital microscope equipped with a VH-Z100 wide range zoom lens. Melt pool boundaries are measured in each of the three cross sections and averaged to determine the displayed values.

4. Probabilistic model calibration approach

In the present work, model calibrations are performed using Bayesian statistical inference based on the Bayes' rule. In this context, the prior probability distribution for the model parameters defined through the prior knowledge from the literature and/or experts, $P(\theta)$, is updated to a posterior distribution, $P(\theta|D)$, by a likelihood function, $P(D|\theta)$. The likelihood compares the model results, $M(\theta)$, and the corresponding data, D, and shows how likely to obtain the data given the parameter values of interest, θ. In this statistical inference process, there are some intractable integrals in order to find the statistical properties of the posterior distribution. These integrals are typically very hard or sometimes impossible to calculate through conventional analytical or numerical techniques due to the curse of high-dimensionality in the parameter space for most scientific models. However, the fast development of computing capabilities through the super-computers over the recent decade has made the numerical MCMC sampling approaches applicable to address the integration problem in the probabilistic calibrations of models, provided they are inexpensive—more sophisticated approaches are necessary when model costs are significant [30].

An adaptive MCMC Metropolis-Hastings (M-H) algorithm is employed to perform the model calibration and uncertainty analysis. This approach begins with an initial guess for the model parameters within the predefined parameter ranges, θ^0, and continues by a sequential sampling of parameter vectors from an adaptive proposal posterior distribution, q. Here, the proposal distribution is considered to be a multivariate Gaussian distribution with a mean vector equal to the previous parameter vector in the MCMC sample chain, θ^{i-1}, and an adaptive variance-covariance matrix, which changes as a function of the variance-covariance matrix obtained from all the previous parameter vectors. The sampled parameter vector at each iteration during the sequential process is considered as a candidate, θ^{cand}, that is accepted or rejected using the following M-H ratio,

$$MH = \frac{P(\theta^{cand})P(D|\theta^{cand})}{P(\theta^{i-1})P(D|\theta^{i-1})}\frac{q(\theta^{i-1}|\theta^{cand})}{q(\theta^{cand}|\theta^{i-1})} \tag{2}$$

where the first and second fractions are known as Metropolis and Hastings ratios, respectively. At each iteration, the Metropolis ratio compares the posterior probability of the candidate with its counterpart for the previous parameter vector in the chain. This comparison is performed through the joint probabilities—i.e., prior $\times$ likelihood—that are proportional to their corresponding posterior probabilities. The Hastings ratio compares the probability of the forward move from the previous parameter vector to the candidate with the probability of the reverse move. The chance of candidate acceptance is $\min\{\mathrm{MH}, 1\} \times 100$. If the candidate acceptance occurs, $\theta^i = \theta^{cand}$; otherwise, $\theta^i = \theta^{i-1}$.

The sampling process continues until the proposal distribution becomes stationary, which is equivalent to parameter convergence. In other words, *the MCMC parameter samples converge to a fixed distribution rather than a constant value*. The parameter samples before convergence is known as the "burn-in period", which is discarded before for the parameter calibration and UQ are done. The distribution of the remaining samples (in the convergence region) can approximately represent the posterior distribution of the model parameters given data. In the context of probabilistic calibration, the mean values and square root of the diagonal terms in the variance-covariance matrix of these parameter samples can also be introduced as the most plausible values for the model parameters and their standard deviations, respectively.

These values and their uncertainties are also propagated to the model outputs—i.e., melt pool width and depth—through model forward analysis. In this UP approach, the model outputs are obtained for each parameter sample in the convergence region; then, 2.5% of the samples are discarded from the upper and lower values of the sorted output samples to provide 95% credible intervals.

5. Results and discussion

5.1. Statistical test of the E-T model

In this section, the MCMC approach described in Section 4 is applied to probabilistically calibrate the uncertain parameters in the E-T model—i.e., μ, κ, and C_p—against extensive experimental data for different material systems described in detail in Section 3. As discussed previously, an exhaustive design of experiments is taken into account to cover a reasonable range of the input controls for each material system, where laser power and velocity can change from almost 40–260 W and 0.05–2.40 m/s, respectively. The corresponding measured data for melt pool depth and width is used for model calibration (75–80% of data) and validation (20–25% of data). It should be noted that melt pool length is not involved in these analyses due to the difficulties in its experimental measurement—it is only measurable through direct imaging of the melt pool during processing, contrary to width and depth, which can be measured *postmortem*. In these probabilistic calibrations, a uniform probability density function (PDF) is considered as the prior PDF for each model parameter. The uniform PDFs for the parameters μ, κ, and C_p are ranged from 0.3 to 0.8, 2–120 W/mK, and 450–2000 J/kgK in a conservative manner. Moreover, fixed values are assigned to the parameters ρ and σ based on the given material system and the experimental laser beam size, $\sigma = d/4$, respectively. It is worth noting that the likelihood function in these analyses is assumed to be a multivariate Gaussian distribution centered at the experimental data vector with a fixed diagonal variance-covariance matrix of the data errors, assuming statistical independence among all the given data for each material system.

The above-mentioned settings are utilized to generate 30,000 MCMC samples of the parameter vectors for the parameter inference in each calibration case. In Fig. 1, the MCMC chain plot for each parameter is shown for the AF9628 case (see supplementary material for all the calibration cases [49]). The red shaded regions in these plots correspond to the burn-in periods before the parameters converge, where there are non-uniform fluctuations of the parameter values.

As mentioned in Section 4, these parameter samples are discarded to find the parameter posterior PDFs. For visualization of the parameter PDFs, marginal and joint (pair) PDFs are plotted in Figs. 2 and 3, respectively. As observed in these plots, the uniform parameter prior PDFs are updated to the peaked posterior PDFs given the training experimental data for the AF9628 system that are used in the parameter inference (see supplementary material for all the calibration cases [49]).

3-D joint PDFs in Fig. 3 can be turned into 2-D color graphs shown in Fig. 4 in order to evaluate the degree of correlation between each pair of parameters (see supplementary material for all the calibration cases [49]). In these graphs, the x and y axes show the parameter space for a given parameter pair, and the color spectrum corresponds to the probability densities in each case. The linear color features in all of these graphs qualitatively indicate strong linear correlations between all three pair parameters. These correlations can also be quantified through the Pearson coefficient, ρ_c, defined as the covariance of the given parameter pair, over their standard deviations—i.e., $\rho_c = \rho_{X,Y} = cov(X,\ Y)/\sigma_X\sigma_Y$. The linear coefficient is bounded between -1 and 1. Coefficient values close to zero indicate no (linear) correlations between the given parameters, whereas the values close to 1 or -1 correspond to very high linear correlations. It is worth noting that the positive and negative signs demonstrate the correlation direction. As shown in supplementary material for Fig. 4 [49], the linear coefficients are positive and mostly above 0.95. These strong correlations between the pair parameters in different systems imply a triple linear correlation between the given three parameters in the E-T model, which are shown in the plot insets of supplementary material for Fig. 4 [49]. In these figure insets, the samples are plotted in each pair parameter space with the colors indicating the values of the third missing parameter. Here, the triple correlations are observed through the linear features of the samples and uniform changes of the colors.

In the context of the probabilistic calibration, the mean values of the parameter samples (after the removal of the burn-in periods) and the square roots of the diagonal elements in their variance-covariance matrix provide the most plausible values, $\overline{\theta}$, and standard deviations, σ_θ, of the model parameters, as shown in Table 1. The mean values for melt pool width and depth corresponding to different experimental conditions are obtained from the model using the mean values of the parameters for each material system. The parameter uncertainties are also propagated to the mentioned melt pool dimensions for both training and test experimental conditions through the forward UP analysis discussed

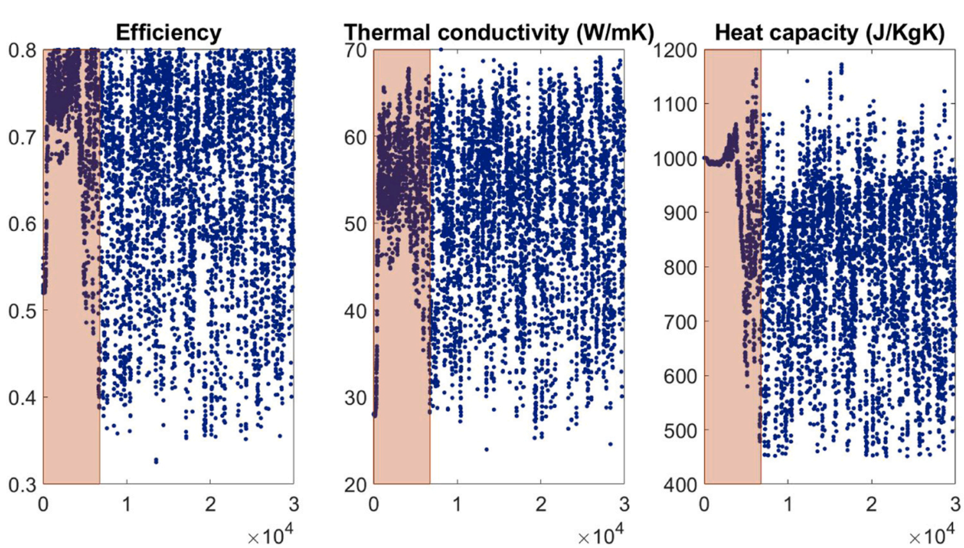

Fig. 1. MCMC chain plots of the model parameters for the ultra-high strength steel AF9628 that shows the burn-in periods in the red shaded regions before the parameters converge (see supplementary material for all the calibration cases [49]). (For interpretation of the references to colour in this figure legend, the reader is referred to the web version of this article.)

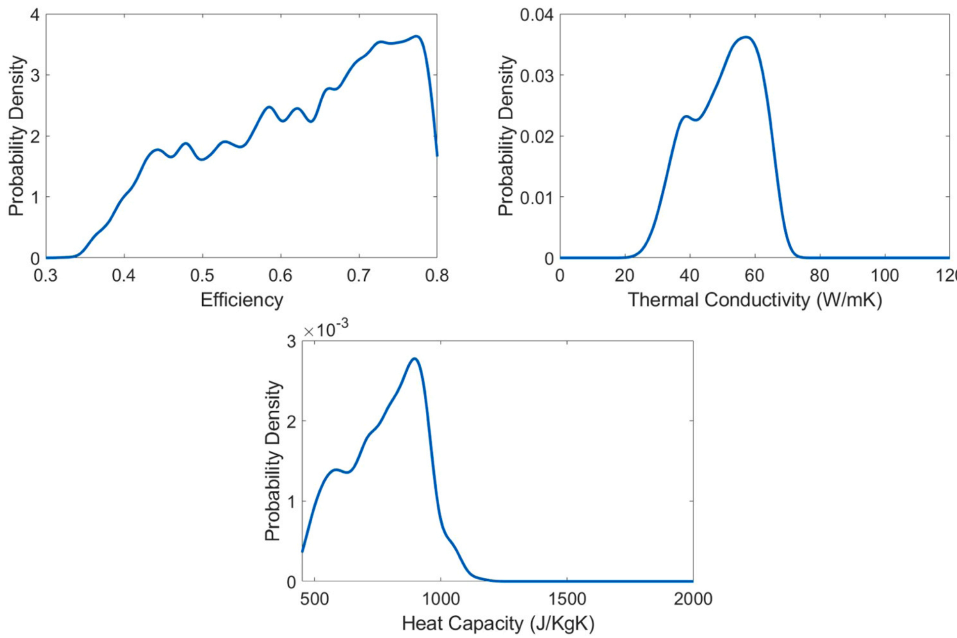

Fig. 2. Marginal parameter posterior PDFs for the ultra-high strength steel AF9628 (see supplementary material for all the calibration cases [49]).

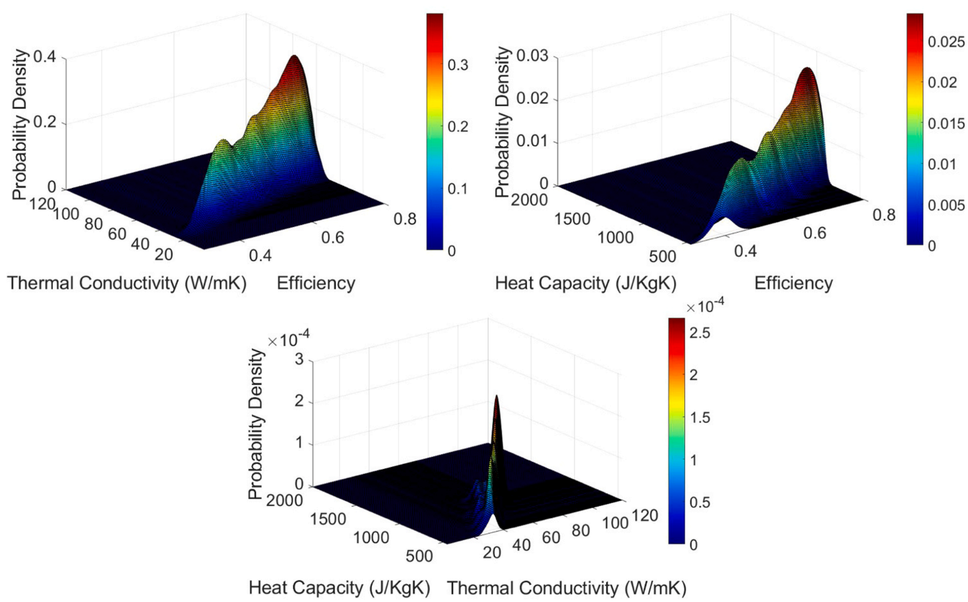

Fig. 3. Joint (pair) parameter posterior PDFs for the ultra-high strength steel AF9628 (see supplementary material for all the calibration cases [49]). Colors show the probability densities. (For interpretation of the references to colour in this figure legend, the reader is referred to the web version of this article.)

in Section 4. These mean values and uncertainties in the form of 95% credible intervals—i.e., $M(\overline{\theta}) \pm 2\sigma_M$—are shown by circles and error bars in Fig. 5. It should be noted that the colors indicate the linear energy density (LED) for each experimental condition—where $LED(J/m) = P(W)/V(m/s)$. In these figures, the calibrated model results are compared with the corresponding experimental data through R-squared (R^2) and Root Mean Square Error (RMSE) metrics in each case. These metrics are expressed as follows,

$$R^2 = 1 - \frac{\sum_{n=1}^{N_D} (D_n - M_n(\overline{\theta}))^2}{\sum_{n=1}^{N_D} (D_n - \overline{D})^2} \tag{3}$$

$$RMSE = \sqrt{\frac{\sum_{n=1}^{N_D} (D_n - M_n(\overline{\theta}))^2}{N_D}} \tag{4}$$

where N_D is the number of given experiments for each applied material system, $M_n(\overline{\theta})$ is the nth calibrated model result—either melt pool width or depth, D_n is the corresponding experimental data, and $\overline{D}$ is the average of all experimental data in each case.

As observed in Fig. 5, all the predictions show some discrepancies with the given experimental data. However, these discrepancies are much more significant for the melt pool depth compared to the width, as can be identified by *the much lower* R^2s and *much larger* RMSEs for the melt pool depth predictions. Closer attention to the results reveals a similar trend in the depth discrepancies for all the given material

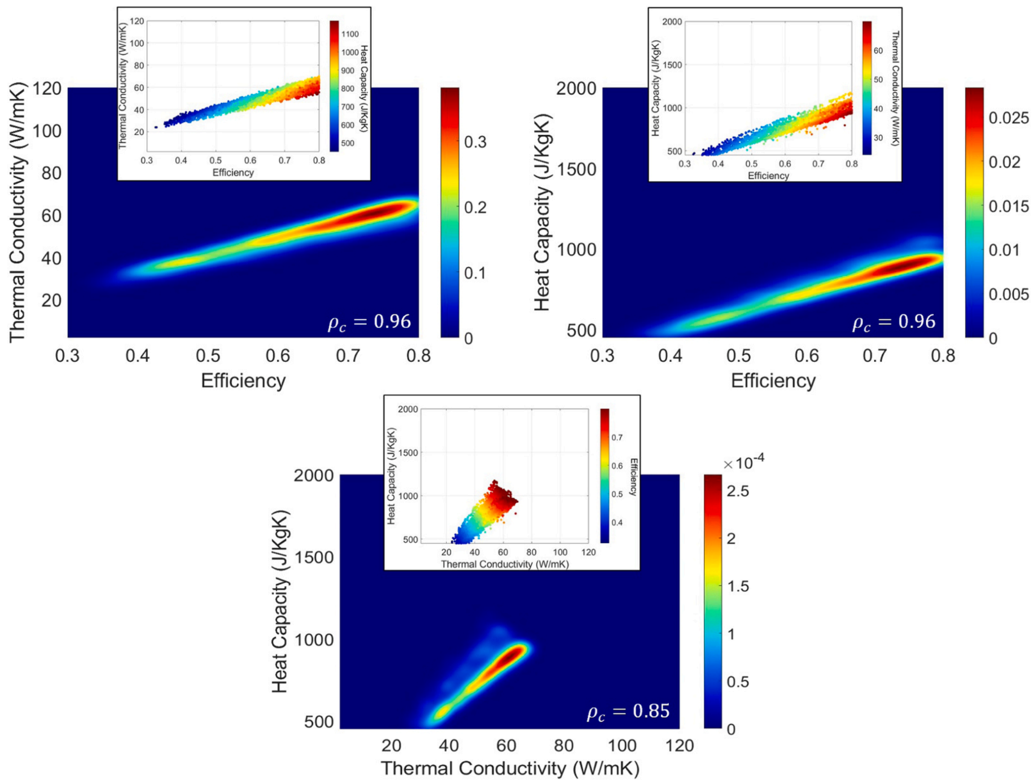

Fig. 4. Linear correlation color graphs for the model parameters in the ultra-high strength steel AF9628 (see supplementary material for all the calibration cases [49]). Colors show the probability densities and the third parameter values for the main graphs and insets, respectively. (For interpretation of the references to colour in this figure legend, the reader is referred to the web version of this article.)

Table 1
MCMC calibrated model parameters and their standard deviations.

	μ	κ (W/mK)	C_p (J/kgK)
AF9628	0.63 ± 0.12	50.6 ± 10.0	776 ± 150
80Ni-20Cu	0.64 ± 0.11	49.7 ± 8.9	831 ± 148
96.8Ni-3.2 Nb	0.65 ± 0.11	40.0 ± 7.0	740 ± 126
51.2Ni-48.8Ti	0.62 ± 0.13	31.5 ± 6.6	954 ± 200

systems. In this regard, the experimental conditions with some specific combinations of high laser powers and low laser velocities—where the depths are at high values—are the main contributors to the large discrepancies for depth. According to the general idea of the printability maps in the AM literature [23,24,50,51], it seems that these conditions mostly correspond to the occurrence of the keyholing phenomenon, which results in larger melt pool depths relative to what would be expected from conduction heating. As will be explained in Section 5.2, during keyholing, the melt pool is further depressed due to recoil pressure arising as a reaction to large evaporative fluxes out of the melt pool into the atmosphere. Since the physics associated with the keyholing phenomenon is not considered in the E-T model, the depth prediction is considerably underestimated for these experimental conditions. For this reason, a parametric, *physics-based* correction is suggested in this work to cover the discrepancy between the melt pool depth prediction and corresponding experimental data when the keyholing occurs during the thermal process.

5.2. Physical correction of melt pool depth under keyholing condition

As mentioned in Section 5.1, keyholing occurs under a combination of sufficiently high heat source power and low scan velocity—the onset of keyholing is highly material dependent. Under this condition, there is not enough time for the substrate to dissipate the energy deposited by the heat source, resulting in a local temperature rise to the boiling point of the material, which in turn produces a large evaporative flux from the melt pool surface. The latter is balanced by a strong recoil pressure into the melt pool surface. This evaporation-induced recoil pressure leads to a deep melt pool penetration that is manifested as a very deep melt pool [52], without noticeably affecting the width of the melt pool that one would predict under conventional conduction-mode melting/solidification. In order to quantitatively analyse this process, Gladush and Smurov [53] proposed a simplified model to predict the melt pool depth, d_k, in terms of the laser power, velocity, and beam size, under keyhole conditions:

$$d_k = \frac{\mu P}{2\pi\kappa T_b} ln\left[\frac{\sigma + (\alpha/v)}{\sigma}\right] \tag{5}$$

where, T_b is the material boiling temperature. This equation was derived by solving the heat conduction problem for a semi-finite flat substrate considering a cylindrical keyhole with radius σ that forms under the heat source.

In this work, the depth discrepancies in Fig. 5 associated with the keyholing conditions are assumed to be proportional to Equation 5. In other words, the multiplication of this expression by a correction factor, C, is taken into account as the depth discrepancy function. An experimentally obtained criterion[23,24] in terms of melt pool dimensions is assumed in this work—as Experimental Width/1.5 $\leq$ Experimental Depth—to recognize the experimental prints that experience the keyholing effect and require the above correction for their depth predictions. In Section 5.3, the MCMC probabilistic calibration is repeated for each material case by considering the keyhole depth's correction factor as an additional parameter.

5.3. Statistical test of the corrected E-T model

In this section, the same MCMC setting is applied to recalibrate the

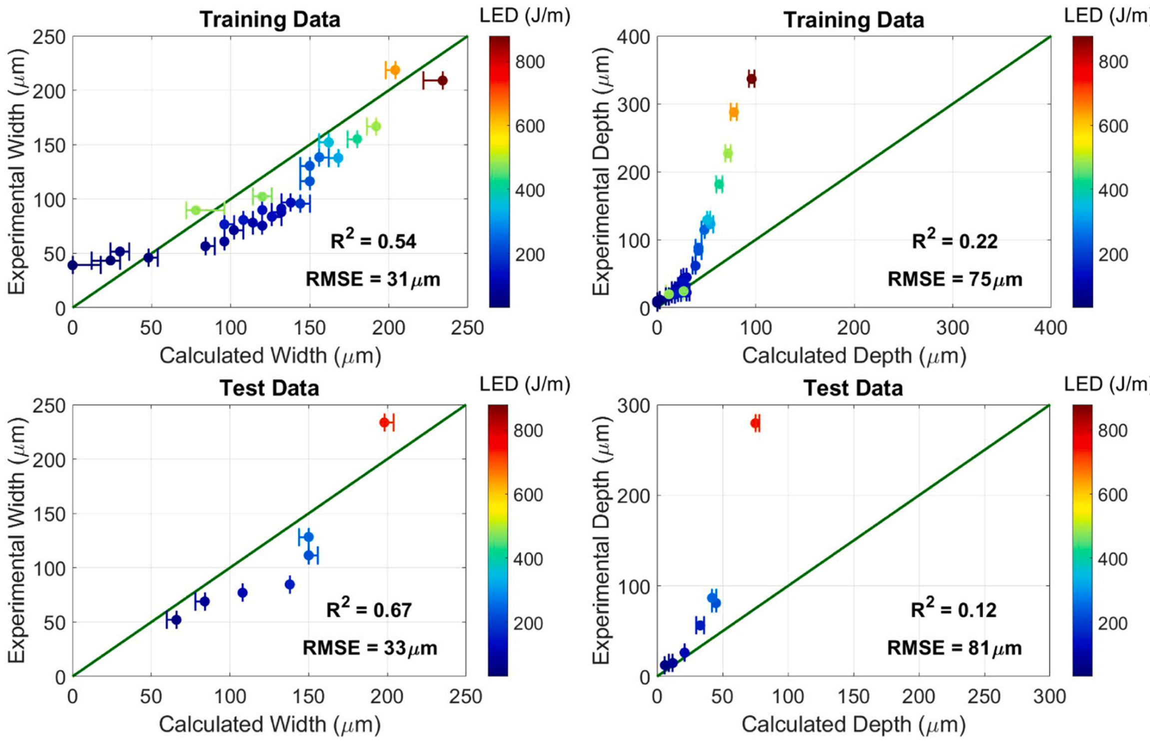

(a) Ultra-high strength steel AF9628

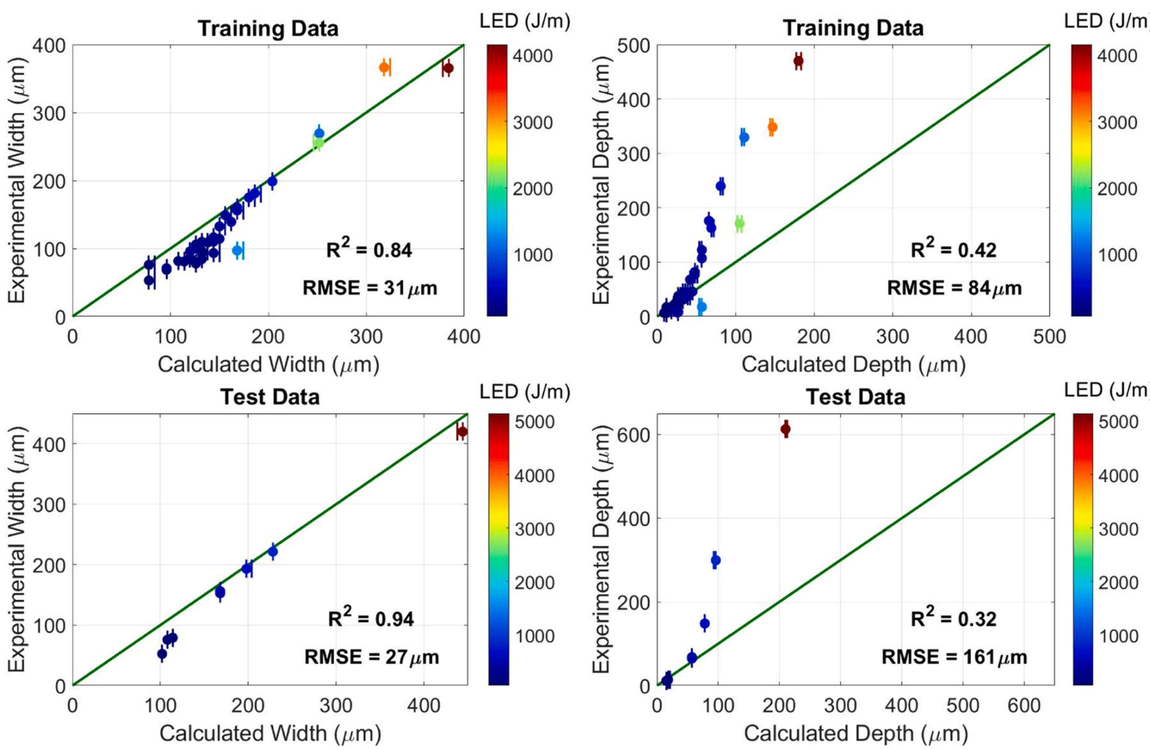

(b) 80Ni-20Cu

Fig. 5. Comparison of the mean value predictions and experimental data for melt pool width and depth at different experimental conditions for each given material system. Error bars are the results of UP through the forward model analysis of calibrated parameters in each case. Colors show the LED values for different experimental conditions. (For interpretation of the references to colour in this figure legend, the reader is referred to the web version of this article.)

model with the additional parameter *C*. Again, a uniform PDF is considered for this parameter, which changes between 1 and 5 for all calibration cases. The MCMC chain plots for all four parameters in the AF9628 case are shown in Fig. 6 (see supplementary material for all the calibration cases [49]). After the removal of burn-in periods in different cases, the parameter analyses are performed by the remaining parameter

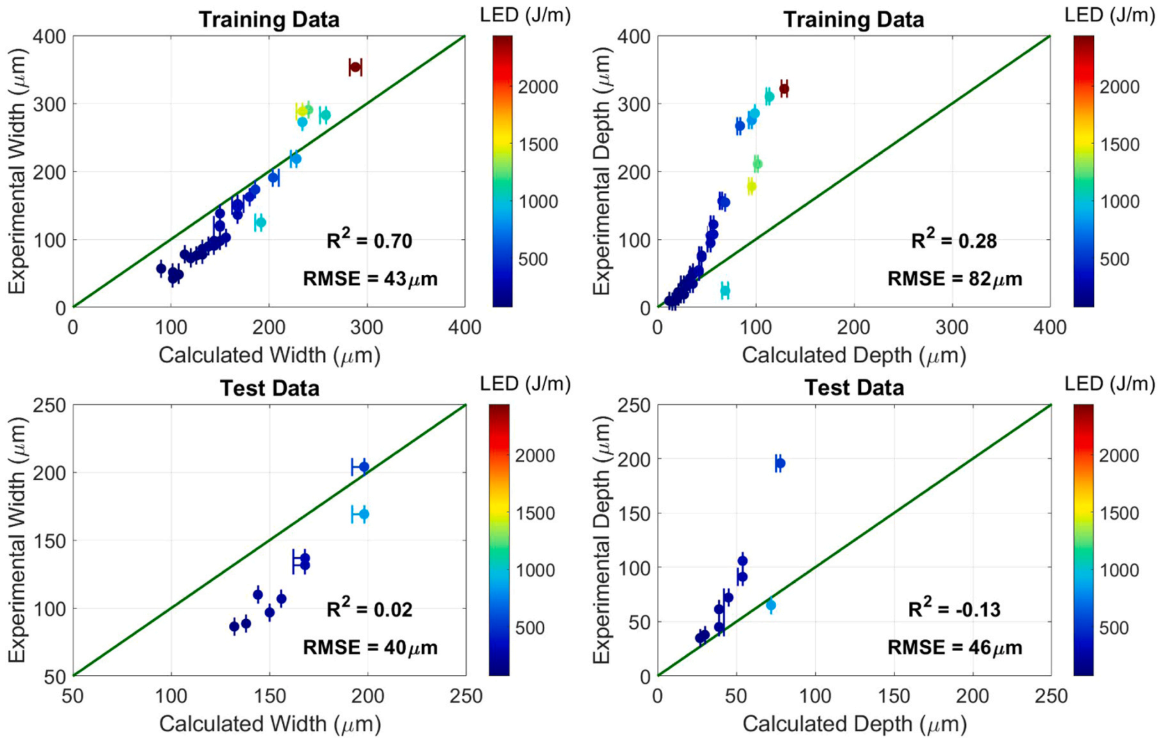

(c) 96.8Ni-3.2Nb

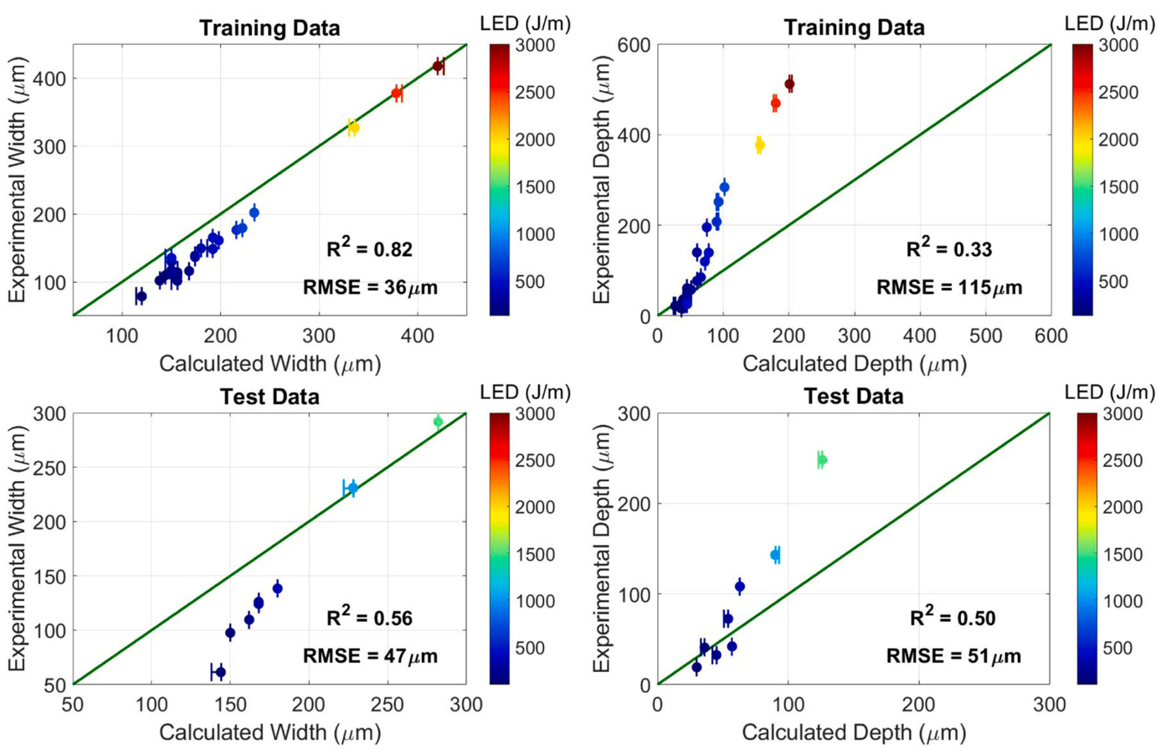

(d) 51.2Ni-48.8Ti

Fig. 5. (*continued*).

vectors in the convergence regions.

The parameter posterior PDFs are evaluated in the form of marginal and joint (pair) posterior PDFs, as shown in Figs. 7 and 8 for AF9628 alloy (see supplementary material for all the calibration cases [49]). These figures indicate that the non-informative uniform distributions turn into relatively informative distributions with peaks after the model calibrations with the corresponding experimental data for the given material systems. Moreover, supplementary material for Fig. 7 [49] clearly shows that the posterior peaks are much more defined for *C* that implies more assertive calibrated values for this parameter.

Again, the correlation graphs for the pair parameters in supplementary material for Fig. 9 [49] show very high linear correlations

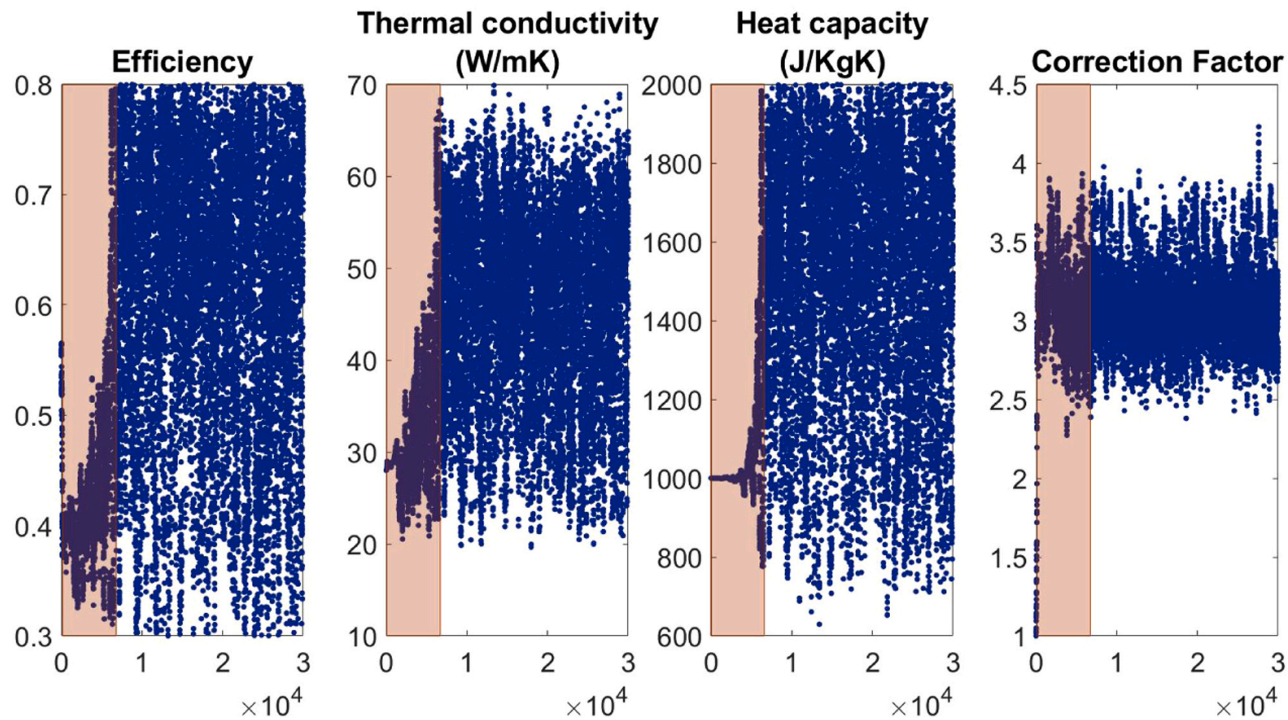

Fig. 6. MCMC chain plots of the parameters for the ultra-high strength steel AF9628 that shows the burn-in periods in the red shaded regions before the parameters converge (see supplementary material for all the calibration cases [49]). (For interpretation of the references to colour in this figure legend, the reader is referred to the web version of this article.)

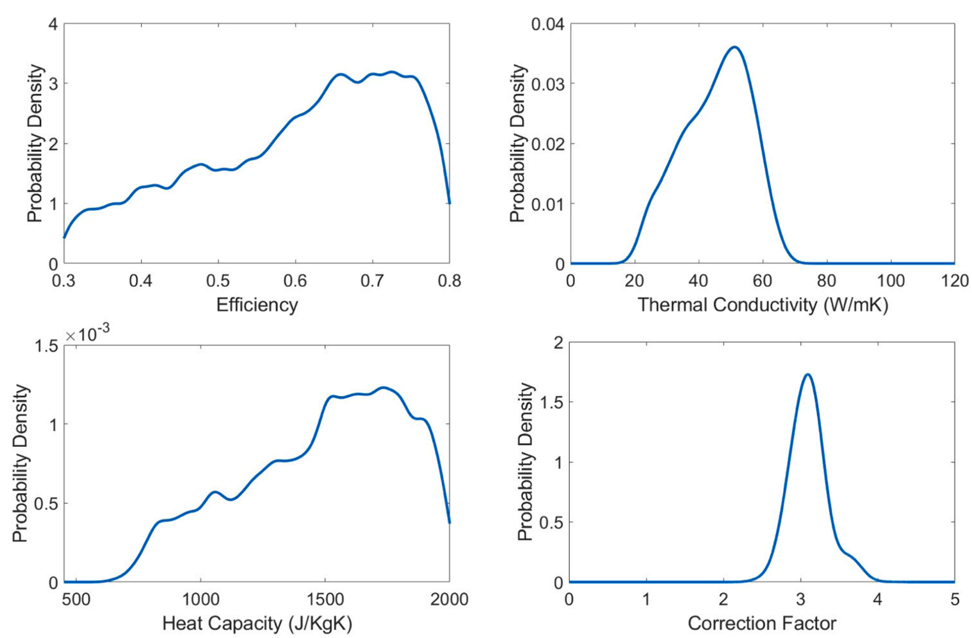

Fig. 7. Marginal parameter posterior PDFs for the ultra-high strength steel AF9628 (see supplementary material for all the calibration cases [49]).

between μ, κ, and C_p in all calibration cases (ρ mostly above 0.9), while there are weak linear correlations between C and these three parameters (ρ mostly between -0.3 and 0.15). These weak correlations indicate that parameter C almost *has an independent contribution in the predictions and cannot be substituted with other parameters*.

For the given material systems, the mean values of the remaining parameter samples (in the convergence regions) and the square roots of the diagonal terms in their variance-covariance matrix are also listed in Table 2 as the most plausible values and standard deviations for the parameters, respectively. Comparing Tables 1 and 2 demonstrates that μ is almost the same for both model calibrations with and without the depth correction factor, whereas κ and C_p undergo some changes, with the latter undergoing the most significant change when the correction for keyholing is included. It can also be observed that the addition of the fourth parameter—i.e., C—provides more flexibility for the other three parameters leading to larger standard deviations or more uncertainty. Moreover, optimal values, greater than 1, have been obtained for the correction factor C in different calibration cases, which result from the

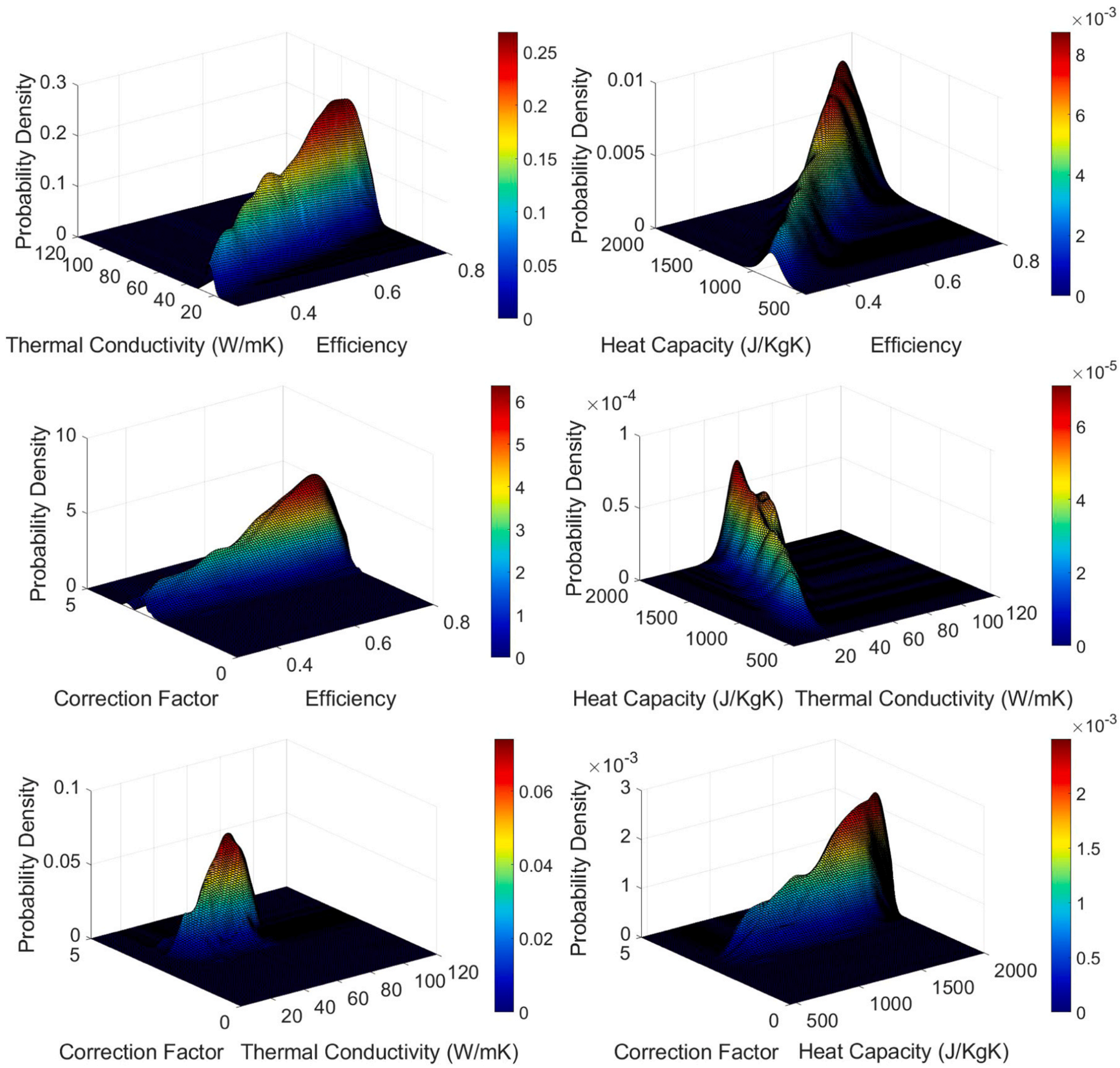

Fig. 8. Joint (pair) parameter posterior PDFs for the ultra-high strength steel AF9628 (see supplementary material for all the calibration cases [49]). Colors show the probability densities. (For interpretation of the references to colour in this figure legend, the reader is referred to the web version of this article.)

underestimation of keyhole depth through the simplified relationship in Equation 5. In the case of AF9628 alloy, a more significant depth underestimation provides a much higher optimal value for C—i.e., a value larger than 3. Nevertheless, under the keyholing conditions, a depth discrepancy function proportional to the formulation in Equation 5 is still a more reasonable and physical assumption compared to a discrepancy function with just a constant term.

At the given training- and test-experimental conditions for each material case, the most optimal values for the model responses and their 95% credible intervals are calculated using the forward model analyses. These optimal results are compared with their corresponding experimental data in Fig. 10. Here, much higher R^2 and lower RMSE values for melt pool depth plots indicate considerably better agreement between the model predictions and experimental data in all the given cases compared to their counterparts obtained from the calibration with no keyholing depth correction in Section 5.1. There is also slightly better agreement for melt pool width predicted for different given materials. This can be attributed to the compromising parameter values obtained after the calibrations with no depth correction for the sake of obtaining the maximum possible depth predictions at keyholing conditions, which is accompanied by more discrepancies for melt pool width. According to Fig. 10, R^2 values are larger than 0.9 and RMSE values are between 19 and 28 μm for the depth predictions associated with the training data. Although the width predictions for the training data show slightly lower values of R^2 and higher values of RMSE, there are still relatively good agreements between the predictions and corresponding data. Moreover, R^2 values greater than 0.55 and 0.8 besides RMSE values smaller than 43 and 33 μm for the width and depth predictions associated with the test data can be acceptable enough to validate the E-T model corrected for the keyholing depth.

Consequently, it seems the biases and underfitting in Fig. 5, resulting from the large melt pool depth underestimations of the original E-T model for the print conditions experiencing keyholing, are resolved after the model correction for the keyholing mode, as shown in Fig. 10. This can be inferred from the predictions at most training data that include the corresponding experimental results in their 95% credible intervals. Also, no overfitting is observed for the corrected model since the predictions at the test data show similar trends and precision to the predictions at the training data. However, it should be noted that the discrepancies between the corrected-model predictions and experimental results can result from the errors associated with the model parameters, the simplification assumptions as well as the missing physics in the model, and the experimental data, as follows:

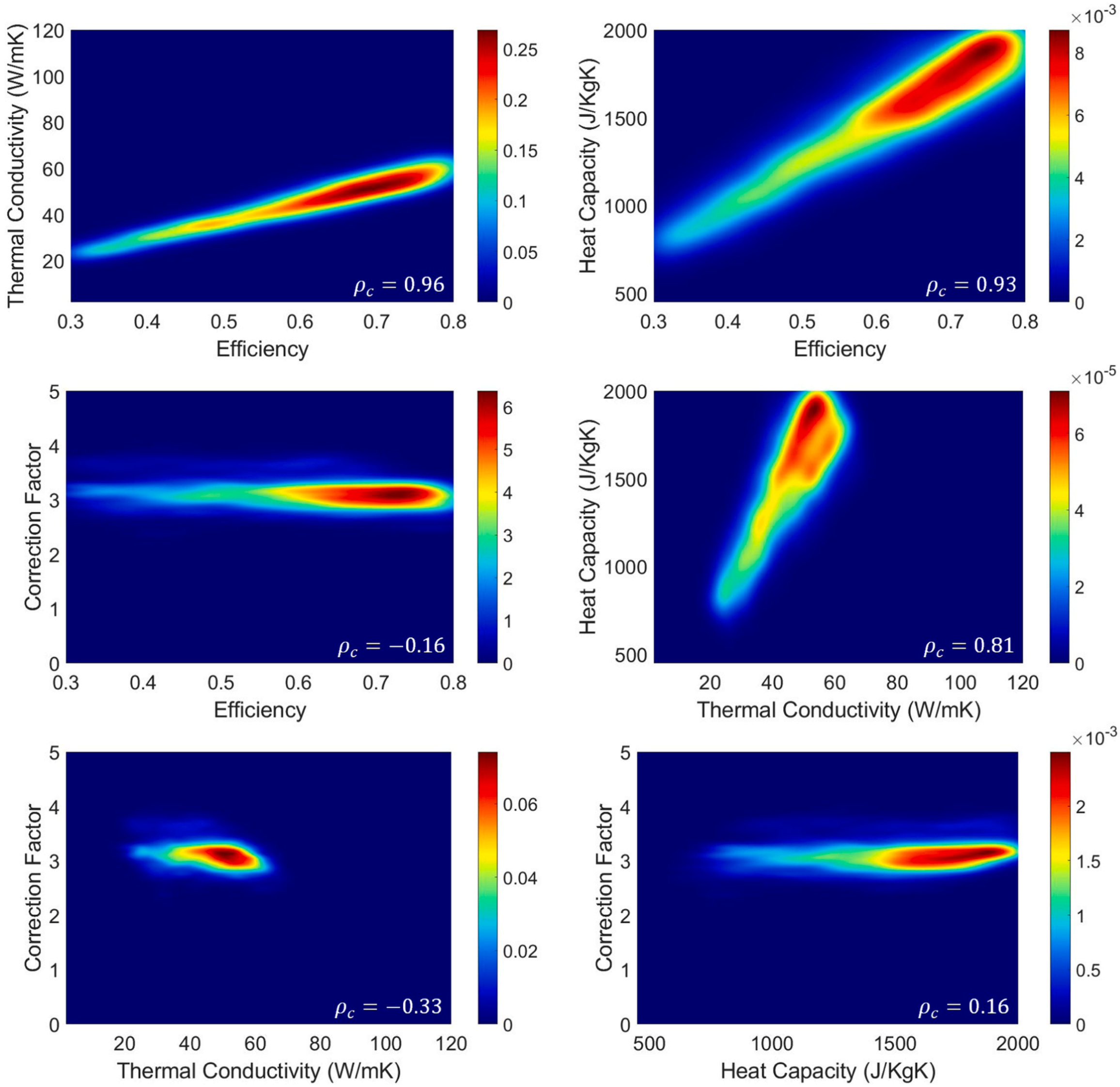

Fig. 9. Linear correlation color graphs for the given parameters in the ultra-high strength steel AF9628 (see supplementary material for all the calibration cases [49]). Colors show the probability densities. (For interpretation of the references to colour in this figure legend, the reader is referred to the web version of this article.)

Table 2
MCMC calibrated model parameters and their standard deviations after the depth correction for the keyholing conditions.

	μ	κ (W/mK)	C_p (J/kgK)	C
AF9628	0.60 ± 0.13	45.2 ± 10.6	1490 ± 324	3.10 ± 0.24
80Ni-20Cu	0.62 ± 0.12	62.3 ± 12.3	849 ± 166	1.32 ± 0.06
96.8Ni-3.2 Nb	0.64 ± 0.11	48.0 ± 8.4	891 ± 148	1.53 ± 0.07
51.2Ni-48.8Ti	0.61 ± 0.13	39.4 ± 8.6	1212 ± 250	1.53 ± 0.05

1. Physical properties are assumed to be temperature independent for the sake of model simplification. However, the contribution of this assumption to the discrepancies is incorporated into the uncertainties quantified for these properties in this work.
2. Latent heat associated with phase changes is assumed to be negligible compared to the sensible heat during the thermal process. However, this might have a small effect on the predictions of the melt pool dimensions.
3. The semi-infinite thick substrate assumption in the model for single-track prints implies that the temperature rise at the substrate locations where are sufficiently far from the laser beam is negligible and can be ignored if the substrate is large enough. However, this might not be true for all the process conditions (especially for melt pool depths since the substrate thickness is usually not large enough). The E-T model can be improved by considering boundary conditions for the substrate dimensions, which is out of the scope of this work.
4. In the thermal model, the moving heat source just over the substrate in the context of welding results in an extra assumption for the application of the model to the AM processes. This assumption offers that heat conduction solely takes place through the substrate, and the thin powder layer and its heat conduction contribution are ignored. Again, the boundary conditions associated with the powder layer should be implemented in the model to reduce the corresponding uncertainties.
5. A spherical Gaussian-distributed heat source with the same standard deviations (σ) along all directions is assumed in this model, while an elliptical Gaussian distribution with different directional standard deviations (σ_x, σ_y, σ_z) seems to be more realistic. This can be also implemented in the integration of Equation 1, similar to Schwalbach et al. work [26].

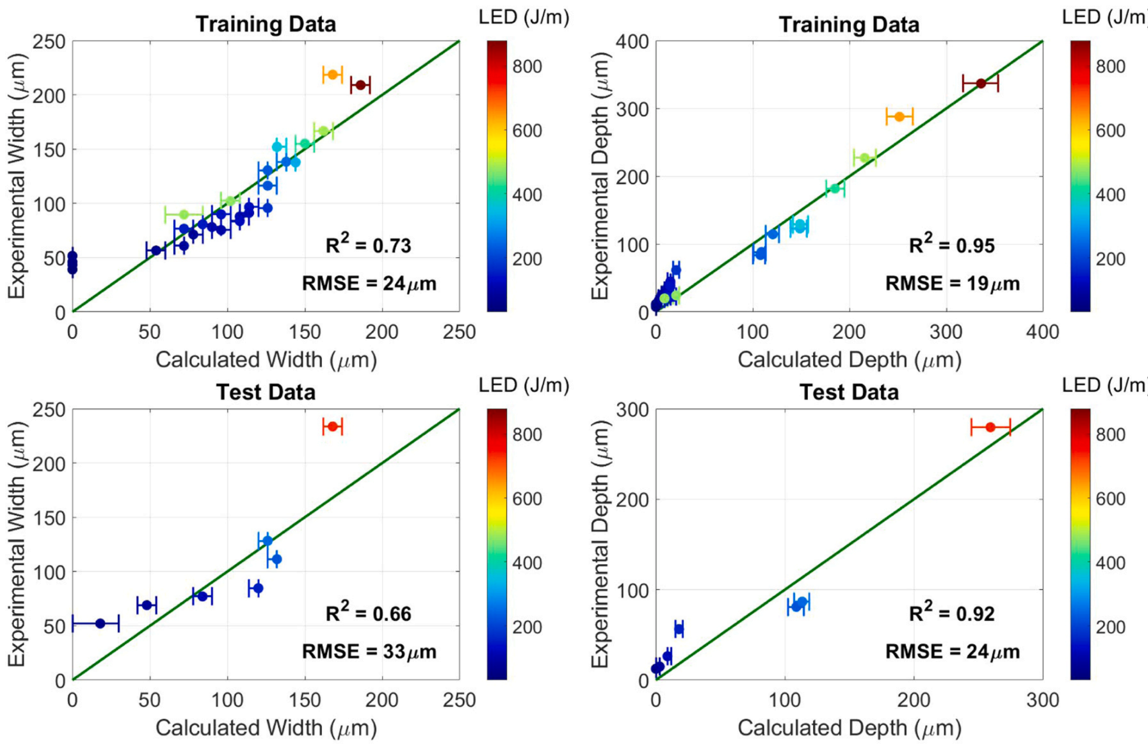

(a) Ultra-high strength steel AF9628

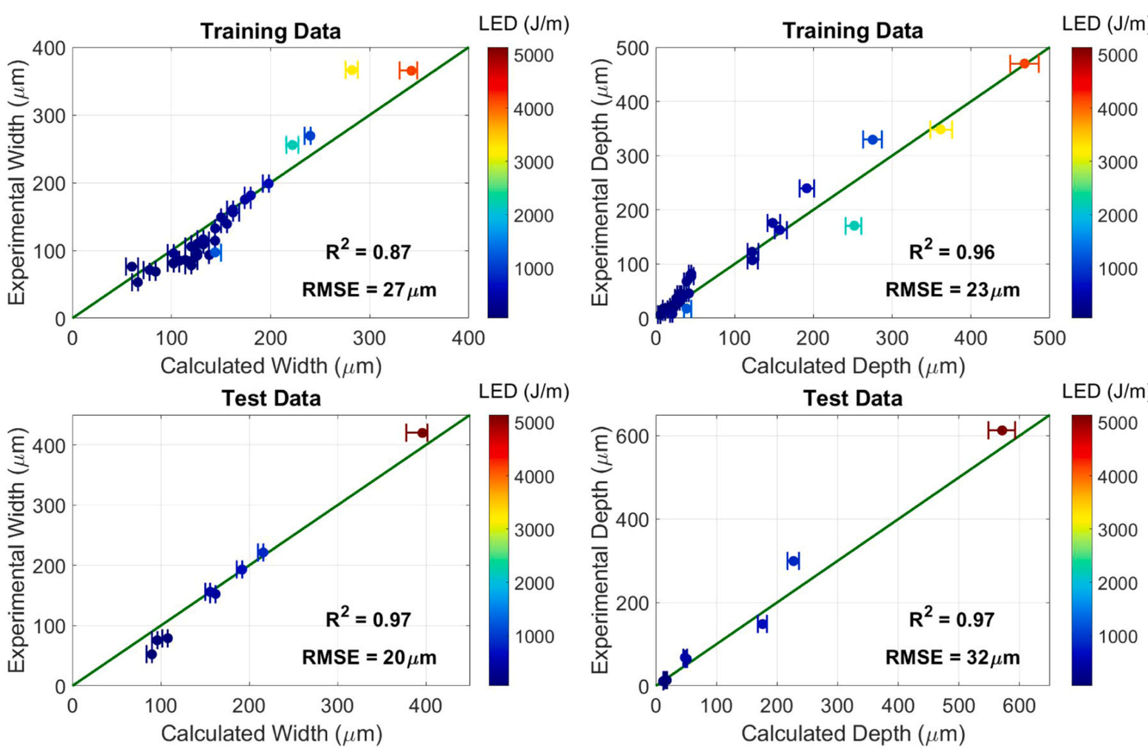

(b) 80Ni-20Cu

Fig. 10. Comparison of the mean value predictions and experimental data for melt pool width and depth at different experimental conditions for each given material system, considering the depth correction for the keyholing conditions. Error bars are the results of UP through the forward model analysis of calibrated parameters in each case. Colors show the LED values for different experimental conditions. (For interpretation of the references to colour in this figure legend, the reader is referred to the web version of this article.)

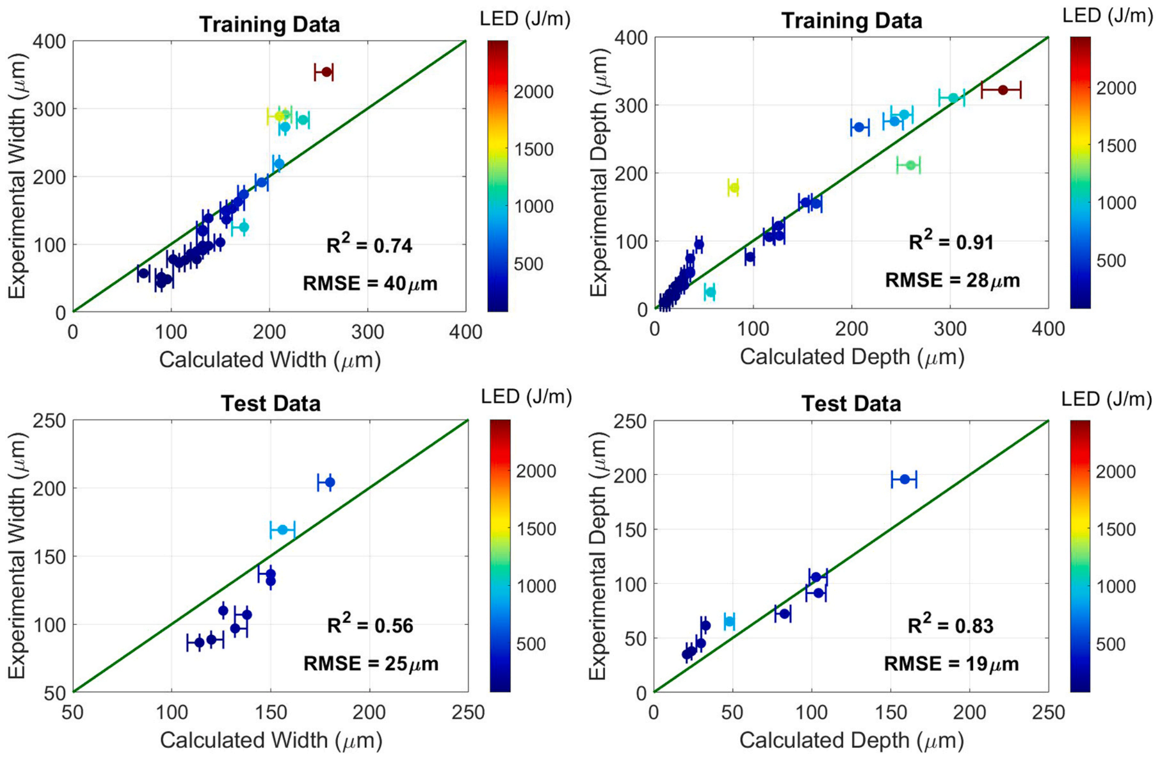

(c) 96.8Ni-3.2Nb

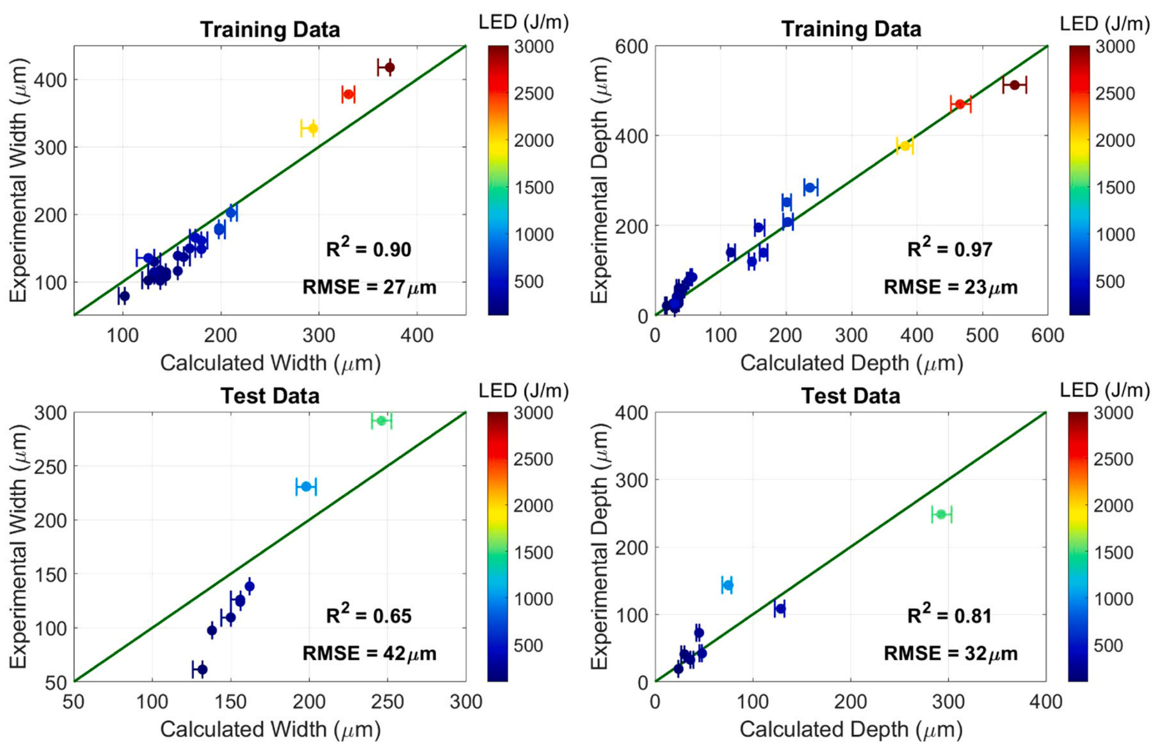

(d) 51.2Ni-48.8Ti

Fig. 10. (*continued*).

6. Lastly, non-uniformity along the prints due to the inevitable instability of the experimental conditions results in high uncertainties in the estimations of the melt pool dimensions.

For more comparisons between the calibrated results obtained for melt pool depth with and without considering the keyholing depth correction and their corresponding experimental data, melt pool depth versus LED is plotted for each material system, as shown in Fig. 11. As observed in the plots, the calibrated results with no depth correction, ones with depth correction, and experimental data are shown by circles, squares, and diamonds, and their trends are illustrated in red, orange, and green lines, respectively. It should be noted that the point sizes and

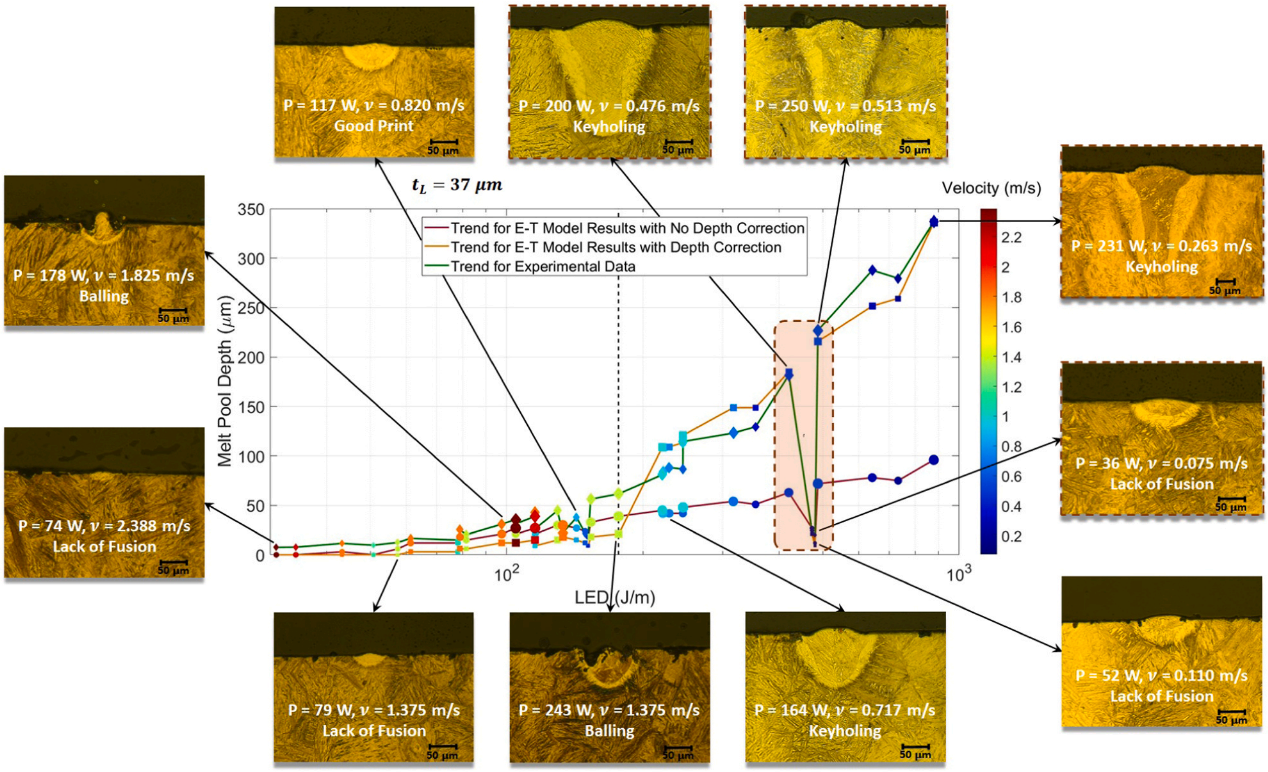

(a) Ultra-high strength steel AF9628

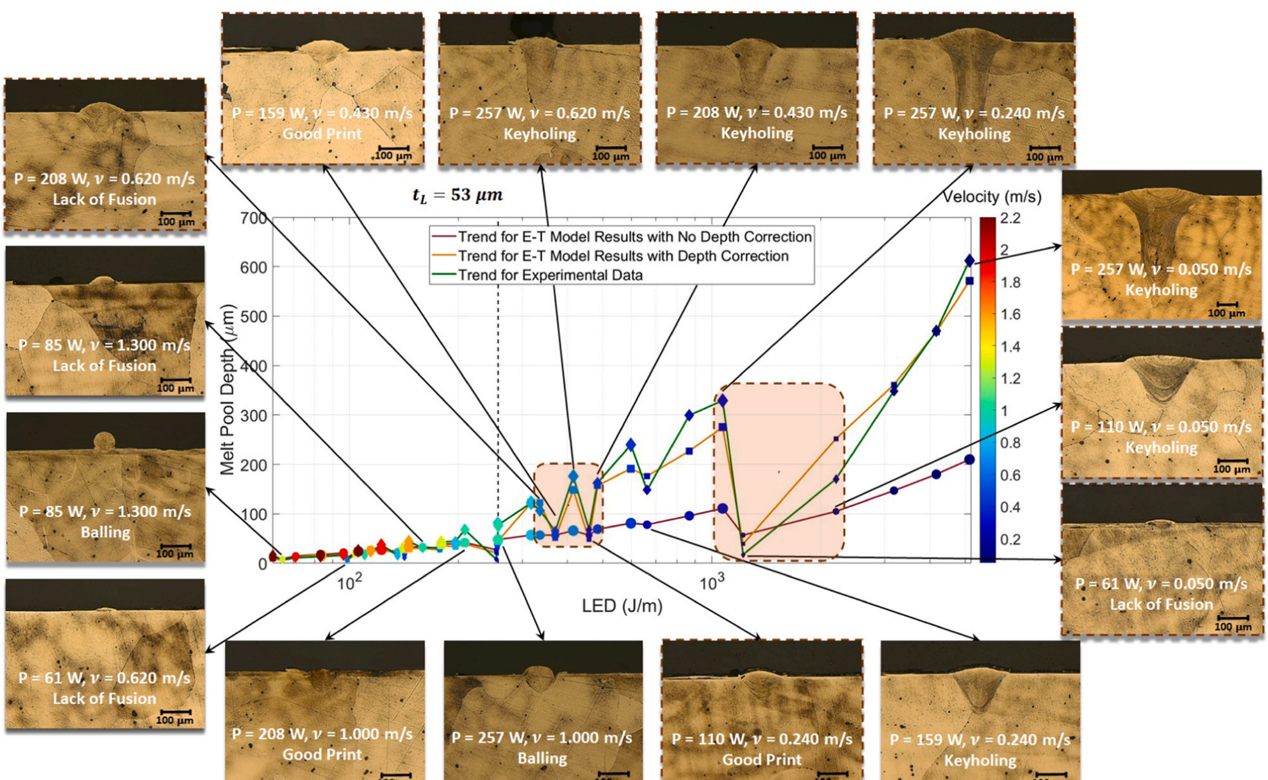

(b) 80Ni-20Cu

Fig. 11. Trends for melt pool depth versus LED obtained from the experiments (green line) as well as calibrations with and without correction (orange and red lines) in different material systems, besides some of the cross-sectional print images. In these plots, point sizes and colors correspond to the laser powers and velocities in the LPBF process. (For interpretation of the references to colour in this figure legend, the reader is referred to the web version of this article.)

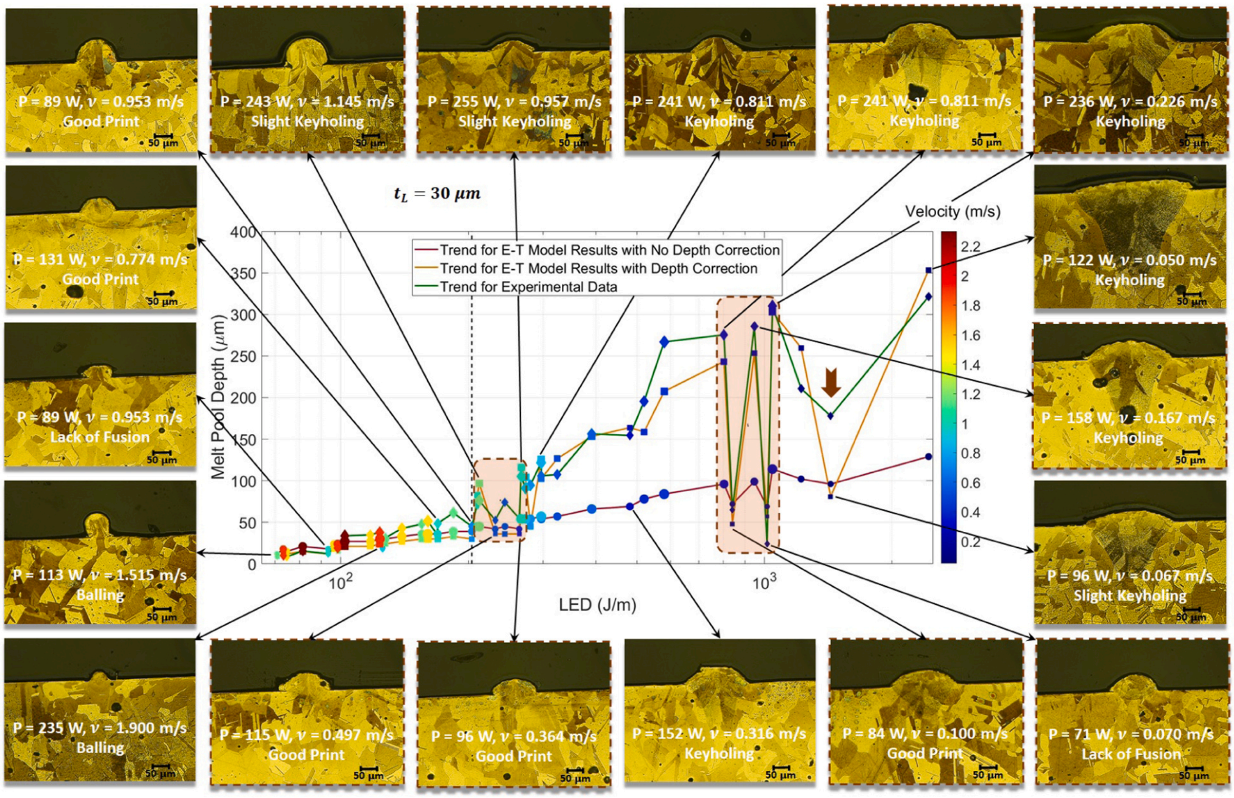

(c) 96.8Ni-3.2Nb

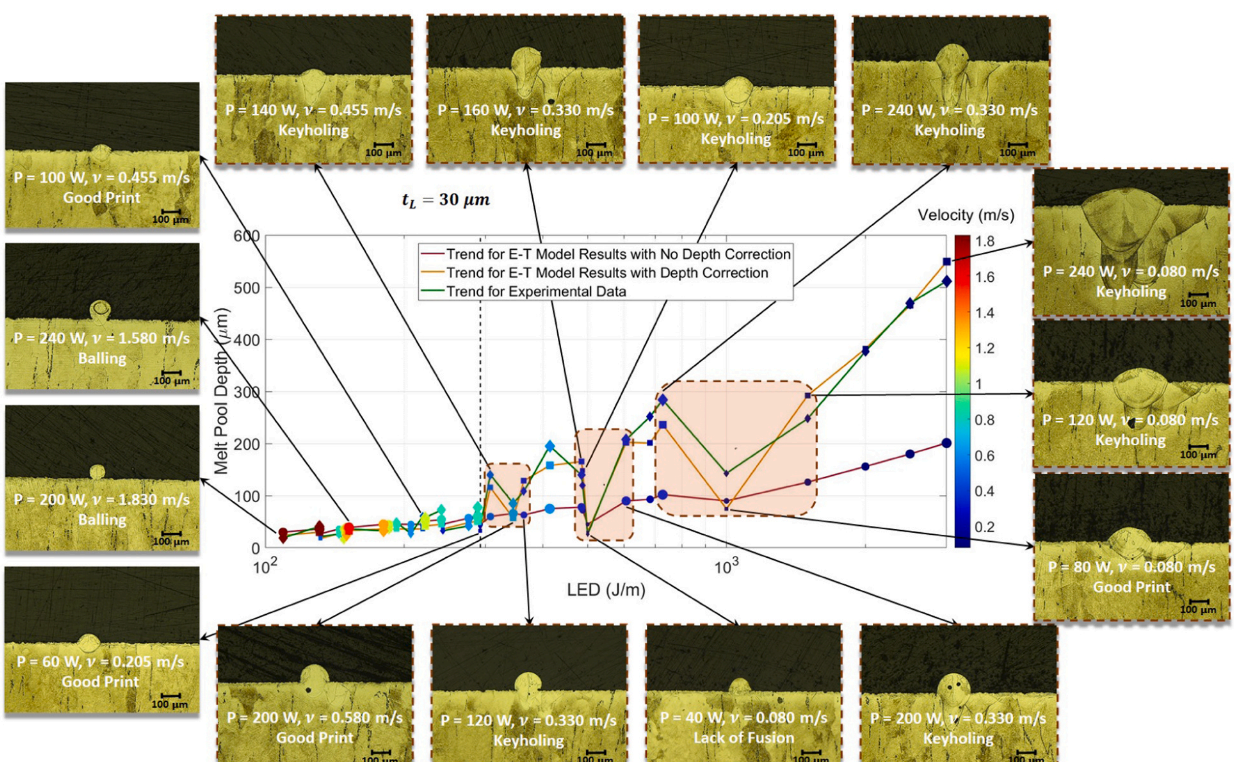

(d) 51.2Ni-48.8Ti

Fig. 11. (*continued*).

colors also represent the laser powers and velocities used in their single-track prints for each material case. Moreover, the LED-axes are shown in the logarithmic scale for better visualization of the results.

As expected, the calibrated results with depth correction show much lower discrepancies and higher trend consistencies with experimental data compared to the calibrated results with no depth correction. The calibrated results with no depth correction are very close to their corresponding experimental data at low LED values, but discrepancies appear as the LED becomes larger than a specific value (shown by a black dotted line) for each given material. Although it seems that there is an increasing trend for these discrepancies as LED increases from the specific value in each plot, it is not necessarily the case for all the experimental conditions with high LED values. Indeed, in these high-LED regions, *there are some drops in the experimental depth values causing zig-zag trends*. At these drops, the calibrated results with no depth correction again become very close to the experimental data, similar to the calibrated results with depth correction.

To explain the experimental trends in the melt pool depth versus LED plots, the physics of heat transfer in the AM processes should be evaluated. In this regard, there are two main factors to determine the temperature profile and melt pool dimension during the AM processes, which are the total energy input density represented by LED and the total energy dissipation per time across the given material controlled by the material's thermal diffusivity. At low LEDs, low energy inputs, which are also tuned down by energy dissipation, prevent melt pool from reaching the material's boiling point or staying at this temperature for a long time, meaning there is no or very low evaporation and thus no keyhole formation under these conditions. Since the physics incorporated into the E-T model can capture this combined effect when there is no keyholing occurrence, both of the calibrated results can be in good agreement with the experimental data. The Cross-sectional images also verify no keyholing effect before the dotted lines (low LEDs) for each given material and show prints experiencing either lack of fusion due to inadequate energy to melt the substrate in depth direction [23] or balling resulting from capillary-based instabilities in the melt pool [23, 24], besides a few good prints with no defects. On the other hand, the high-LED experimental conditions with sufficiently high laser powers can experience a high energy concentration under the melt pool due to the material inability for heat dissipation during the thermal process. Regarding the recognition of print modes through the cross-sectional images, it should be mentioned that while balling and keyholing modes are typically clear from the cross-sectional print appearance, lack of fusion and good quality can be very close in appearance. Here, the lack of fusion mode is differentiated when melt pool depth is smaller or equal to the layer thickness, t_L.

As mentioned in Section 5.2, the concentrated heat raises the melt pool temperature to the boiling point that causes excessive evaporation and the keyhole formation. Therefore, only the calibrated results with depth correction can almost follow the experimental data at these conditions since the E-T model with no depth correction disregards the physics associated with the keyholing effect. However, the high-LED experimental conditions with low laser powers undergo no keyholing phenomenon during their thermal process, which drops the depth values close to the calibrated values with no depth correction. It should be noted that the calibrated results with depth correction mostly follow the drops since the dimensional criterion for keyholing mentioned in Section 5.1 is not satisfied, meaning the depth is calculated just by the E-T model with no additional correction. Again, the cross-sectional images verify the keyholing occurrence after the dotted line for each material case, except for the drops which correspond to either good prints or prints undergoing lack of fusion. However, there is one major drop (the second to last point indicated by the red arrow in Fig. 11c) in the case of 96.8Ni-3.2 Nb that shows a conflict between the prediction based on the mentioned dimensional criterion and the corresponding experiment in experiencing keyholing effect.

Generally, it is interesting that the print mode suddenly changes from keyholing to lack of fusion or good quality and vice versa at these high-LED regions, as observed in the red dotted frames in the plots. These drops can be attributed to sufficiently low velocities at the mentioned conditions that can provide enough time for sufficient heat dissipation across the material in order to prevent temperature rise to the boiling point, despite a high supply of the energy input density resulted from these low velocities. But, even very low velocities with the provision of longer dissipation times cannot stop keyhole formation at sufficiently high laser powers due to extremely high energy input provided by these process conditions. Hence, there is a minimum laser power at each given low velocities, under which no keyholing occurs. This critical value is material dependent, and controlled by the material's thermal diffusivity. No keyholing effect under the critical laser power at each given velocity can also be confirmed by the printability maps [23,24,50,51]. Consequently, the plots in Fig. 11 suggest that LED (the total energy input density) ***is not a good metric to recognize the keyholing conditions***; instead, a trade-off between the total energy input and dissipation rate should be taken into account for this purpose. This combined effect can also be represented in the form of dimensional criteria, such as what is used in this work.

6. Summary and conclusion

In the present work, the E-T model as one of the most commonly used thermal model in AM is statistically evaluated against clean and extensive experimental data for four different material systems. For this purpose, an adaptive MCMC-MH sampling approach in the context of Bayesian statistics is applied to probabilistically calibrate the model parameters—i.e., μ, κ, and C_p—given 75–80% of the experimental data as training data in each case. The rest of the experimental data are used as test data. The parameter samples in the first batch of calibrations show a very high triple linear correlation between the model parameters. In addition, the calibrated model results for the melt pool width have a much better agreement with their corresponding experimental data (both training and test data) compared to the melt pool depth in all four material systems. The discrepancies for the depths mostly result from the model underestimations at combinations of high laser powers and low velocities, which are associated with the occurrence of the keyholing phenomenon. In these experimental conditions, the evaporation-induced pressure on the melt pool surface leads to deep melt pool penetration and increased depth. To reduce these discrepancies, the E-T model is physically corrected for the keyhole depth and statistically tested through another batch of calibrations where the correction factor C is considered besides the other three model parameters. Again, the parameter samples in these calibrations indicate that the three model parameters are still strongly correlated, but they are almost uncorrelated to the parameter C that makes this parameter irreplaceable by any of the other mentioned parameters. The results for melt pool width and depth obtained from the second batch of calibrations become much closer to the training or test experimental data considered for each given material. Therefore, the E-T model with keyhole depth correction demonstrates much higher validity compared to the E-T model with no correction. These comparisons are studied further through the depth-LED plots and cross-sectional print images. The plots show that while both of the calibrated depth trends with or without correction are very consistent with their experimental counterparts at low LED values, the depths obtained from the E-T model with correction follow the experimental trends better at high LED values. The cross-sectional images also demonstrate that lack of fusion and balling are two melting modes observed the most at low LEDs in all the cases, whereas keyholing mostly occurs at high LEDs and contributes as the main source of discrepancies between the calibrated results with no correction for E-T depth and corresponding experimental data. However, there are experimental conditions with high LED that experience no keyholing and instead show prints with lack of fusion or good quality. These conditions correspond to combinations of very low powers and velocities, where despite high total energy inputs (high LEDs), the low velocities provide enough time for the substrate to dissipate heat arisen from low powers and consequently prevent heat concentration and keyholing. Here, both of the calibrated results for melt pool depth again become close to the experimental data at these conditions. According to these analyses and observations, it can be concluded that a combination of total energy input and dissipation should be taken into account to identify the keyholing phenomenon, not just total energy input represented by LED.

The calibrated results generally show that the E-T model has good estimations of melt pool dimensions for all the melting modes—i.e., lack of fusion, balling, and good quality—except for the depth prediction in the keyholing mode that has been physically corrected in this work. Despite some discrepancies between the model predictions and experimental results due to uncertainties corresponding to the parameters, model assumptions plus missing physics, and experimental measurements plus non-uniformity along the prints, the UQ of the corrected E-T model makes this model applicable for product design given the properties of interest. The relatively good validity in terms of accuracy and trend for the corrected model based on experimentally derived information about the keyholing occurrence—i.e., keyholing regions in the experimentally obtained printability maps—implies a promising future for more precise analytical predictions of thermal histories during the AM processes by adding more physics to the model. In the end, it is worth noting that all the above thorough analyses, comparisons, and conclusions could not be achieved without the extensive design of experiments and the availability of high quality data over a wide region of the processing space.

CRediT authorship contribution statement

Pejman Honarmandi: Conceptualization, Formal analysis (UQ/UP), Methodology, Visualization, Validation, Writing – original draft, Writing – review & editing. **Raiyan Seede:** Experimentation, Writing – original draft. **Lei Xue:** Experimentation, Writing – original draft. **David Shoukr:** Thermal modeling. **Peter Morcos:** Thermal modeling. **Bing Zhang:** Experimentation. **Chen Zhang:** Experimentation. **Alaa Elwany:** Supervision, Funding acquisition, Writing – review & editing. **Ibrahim Karaman:** Supervision, Funding acquisition, Writing - review & editing. **Raymundo Arroyave:** Supervision, Funding acquisition, Writing – review & editing.

Declaration of Competing Interest

The authors declare that they have no known competing financial interests or personal relationships that could have appeared to influence the work reported in this paper.

Acknowledgements

The authors would like to acknowledge the support of the Army Research Office (ARO), United States, under Contract No. W911NF-18–1-0278. PH and RA also acknowledge the support of NSF, United States, through Grant No. 1849085. AE acknowledges the support from NSF, United States, through Grant No. 1846676. Portions of this research were conducted with the advanced computing resources provided by Texas A&M High Performance Research Computing. The authors would like to acknowledge the support from Dr. Sean Gibbons and Dr. Philip Flater at AFRL for providing the raw AF9628 material. RA would like to dedicate this manuscript to his former Ph.D. advisor, Prof. Thomas W. Eagar.

Appendix A. Supporting information

Supplementary data associated with this article can be found in the online version at doi:10.1016/j.addma.2021.102300.

References

[1] T.J. Horn, O.L. Harrysson, Overview of current additive manufacturing technologies and selected applications, Sci. Prog. 95 (3) (2012) 255–282.
[2] Y. Huang, M.C. Leu, J. Mazumder, A. Donmez, Additive manufacturing: current state, future potential, gaps and needs, and recommendations, J. Manuf. Sci. Eng. 137 (1).
[3] M. Attaran, The rise of 3-D printing: the advantages of additive manufacturing over traditional manufacturing, Bus. Horiz. 60 (5) (2017) 677–688.
[4] J.C. Steuben, A.J. Birnbaum, J.G. Michopoulos, A.P. Iliopoulos, Enriched analytical solutions for additive manufacturing modeling and simulation, Addit. Manuf. 25 (2019) 437–447.
[5] P. Foteinopoulos, A. Papacharalampopoulos, P. Stavropoulos, On thermal modeling of additive manufacturing processes, CIRP J. Manuf. Sci. Tech. 20 (2018) 66–83.
[6] P. Yuan, D. Gu, Molten pool behaviour and its physical mechanism during selective laser melting of TiC/AlSi10Mg nanocomposites: simulation and experiments, J. Phys. D: Appl. Phys. 48 (3) (2015), 035303.
[7] D. Dai, D. Gu, Thermal behavior and densification mechanism during selective laser melting of copper matrix composites: simulation and experiments, Mater. Des. 55 (2014) 482–491.
[8] S. Mohanty, J.H. Hattel, Numerical model based reliability estimation of selective laser melting process, Phys. Procedia 56 (2014) 379–389.
[9] K. Karayagiz, A. Elwany, G. Tapia, B. Franco, L. Johnson, J. Ma, I. Karaman, R. Arroyave, Numerical and experimental analysis of heat distribution in the laser powder bed fusion of Ti-6Al-4V, IISE Trans. 51 (2) (2019) 136–152.
[10] P. Promoppatum, S.-C. Yao, P.C. Pistorius, A.D. Rollett, P.J. Coutts, F. Lia, R. Martukanitz, Numerical modeling and experimental validation of thermal history and microstructure for additive manufacturing of an inconel 718 product, Prog. Addit. Manuf. 3 (1–2) (2018) 15–32.
[11] B. Schoinochoritis, D. Chantzis, K. Salonitis, Simulation of metallic powder bed additive manufacturing processes with the finite element method: a critical review, Proc. Inst. Mech. Eng., Part B: J. Eng. Manuf. 231 (1) (2017) 96–117.
[12] D. Gu, B. He, Finite element simulation and experimental investigation of residual stresses in selective laser melted Ti-Ni shape memory alloy, Comput. Mater. Sci. 117 (2016) 221–232.
[13] Y. Huang, L. Yang, X. Du, Y. Yang, Finite element analysis of thermal behavior of metal powder during selective laser melting, Int. J. Therm. Sci. 104 (2016) 146–157.
[14] S.A. Khairallah, A.T. Anderson, A. Rubenchik, W.E. King, Laser powder-bed fusion additive manufacturing: physics of complex melt flow and formation mechanisms of pores, spatter, and denudation zones, Acta Mater. 108 (2016) 36–45.
[15] L.-E. Loh, C.-K. Chua, W.-Y. Yeong, J. Song, M. Mapar, S.-L. Sing, Z.-H. Liu, D.-Q. Zhang, Numerical investigation and an effective modelling on the selective laser melting (SLM) process with aluminium alloy 6061, Int. J. Heat. Mass Transf. 80 (2015) 288–300.
[16] P. Michaleris, Modeling metal deposition in heat transfer analyses of additive manufacturing processes, Finite Elem. Anal. Des. 86 (2014) 51–60.
[17] Y. Li, D. Gu, Parametric analysis of thermal behavior during selective laser melting additive manufacturing of aluminum alloy powder, Mater. Des. 63 (2014) 856–867.
[18] F. Liu, Q. Zhang, W. Zhou, J. Zhao, J. Chen, Micro scale 3D FEM simulation on thermal evolution within the porous structure in selective laser sintering, J. Mater. Process. Technol. 212 (10) (2012) 2058–2065.
[19] I.A. Roberts, C. Wang, R. Esterlein, M. Stanford, D. Mynors, A three-dimensional finite element analysis of the temperature field during laser melting of metal powders in additive layer manufacturing, Int. J. Mach. Tools Manuf. 49 (12–13) (2009) 916–923.
[20] L. Dong, A. Makradi, S. Ahzi, Y. Remond, Three-dimensional transient finite element analysis of the selective laser sintering process, J. Mater. Process. Tech. 209 (2) (2009) 700–706.
[21] R.B. Patil, V. Yadava, Finite element analysis of temperature distribution in single metallic powder layer during metal laser sintering, Int. J. Mach. Tools Manuf. 47 (7–8) (2007) 1069–1080.
[22] S. Kolossov, E. Boillat, R. Glardon, P. Fischer, M. Locher, 3D FE simulation for temperature evolution in the selective laser sintering process, Int. J. Mach. Tools Manuf. 44 (2–3) (2004) 117–123.
[23] L. Johnson, M. Mahmoudi, B. Zhang, R. Seede, X. Huang, J.T. Maier, H.J. Maier, I. Karaman, A. Elwany, R. Arróyave, Assessing printability maps in additive manufacturing of metal alloys, Acta Mater. 176 (2019) 199–210.
[24] R. Seede, D. Shoukr, B. Zhang, A. Whitt, S. Gibbons, P. Flater, A. Elwany, R. Arroyave, I. Karaman, An ultra-high strength martensitic steel fabricated using selective laser melting additive manufacturing: densification, microstructure, and mechanical properties, Acta Mater. 186 (2020) 199–214.
[25] D. Rosenthal, The Theory Of Moving Sources Of Heat And Its Application Of Metal Treatments, in: Trans, 68, ASME, 1946, pp. 849–866.
[26] E.J. Schwalbach, S.P. Donegan, M.G. Chapman, K.J. Chaput, M.A. Groeber, A discrete source model of powder bed fusion additive manufacturing thermal history, Addit. Manuf. 25 (2019) 485–498.
[27] T. Eagar, N. Tsai, et al., Temperature fields produced by traveling distributed heat sources, Weld. J. 62 (12) (1983) 346–355.
[28] P. Honarmandi, R. Arróyave, Uncertainty quantification and propagation in computational materials science and simulation-assisted materials design, Integr. Mater. Manuf. Innov. (2020) 1–41.

[29] P. Honarmandi, N.H. Paulson, R. Arróyave, M. Stan, Uncertainty quantification and propagation in CALPHAD modeling, Model. Simul. Mater. Sci. Eng. 27 (3) (2019), 034003.
[30] V. Attari, P. Honarmandi, T. Duong, D.J. Sauceda, D. Allaire, R. Arroyave, Uncertainty propagation in a multiscale CALPHAD-reinforced elastochemical phase-field model, Acta Mater. 183 (2020) 452–470.
[31] P. Honarmandi, L. Johnson, R. Arroyave, Bayesian probabilistic prediction of precipitation behavior in Ni-Ti shape memory alloys, Comput. Mater. Sci. 172 (2020), 109334.
[32] P. Honarmandi, T.C. Duong, S.F. Ghoreishi, D. Allaire, R. Arroyave, Bayesian uncertainty quantification and information fusion in CALPHAD-based thermodynamic modeling, Acta Mater. 164 (2019) 636–647.
[33] P. Honarmandi, A. Solomou, R. Arroyave, D. Lagoudas, Uncertainty quantification of the parameters and predictions of a phenomenological constitutive model for thermally induced phase transformation in Ni-Ti shape memory alloys, Model. Simul. Mater. Sci. Eng. 27 (3) (2019), 034001.
[34] A.A. Talapatra, S. Boluki, P. Honarmandi, A. Solomou, G. Zhao, S.F. Ghoreishi, A. Molkeri, D. Allaire, A. Srivastava, X. Qian, et al., Experiment design frameworks for accelerated discovery of targeted materials across scales, Front. Mater. 6 (2019) 82.
[35] P. Honarmandi, R. Arroyave, Using bayesian framework to calibrate a physically based model describing strain-stress behavior of TRIP steels, Comput. Mater. Sci. 129 (2017) 66–81.
[36] T.C. Duong, R.E. Hackenberg, A. Landa, P. Honarmandi, A. Talapatra, H.M. Volz, A. Llobet, A.I. Smith, G. King, S. Bajaj, et al., Revisiting thermodynamics and kinetic diffusivities of uranium-niobium with bayesian uncertainty analysis, Calphad 55 (2016) 219–230.
[37] P. Voorhees, G. Spanos, et al., Modeling across scales: a roadmapping study for connecting materials models and simulations across length and time scales, Tech. rep., Tech. rep., Tech. rep., The Minerals, Metals & Materials Society (TMS) (2015).
[38] R. Arróyave, D.L. McDowell, Systems approaches to materials design: past, present, and future, Annu. Rev. Mater. Res. 49 (2019) 103–126.
[39] Z. Hu, S. Mahadevan, Uncertainty quantification in prediction of material properties during additive manufacturing, Scr. Mater. 135 (2017) 135–140.
[40] F. Lopez, P. Witherell, B. Lane, Identifying uncertainty in laser powder bed fusion additive manufacturing models, J. Mech. Des. 138 (11).
[41] C. Kamath, Data mining and statistical inference in selective laser melting, Int. J. Adv. Manuf. Technol. 86 (5–8) (2016) 1659–1677.
[42] P. Nath Z. Hu S. Mahadevan Multi-level uncertainty quantification in additive manufacturing Proc. 28th Annu. Int. Solid Free. Fabr. Symp. . - Addit. Manuf. Conf. 2017 922 937.
[43] G. Tapia, W. King, L. Johnson, R. Arroyave, I. Karaman, A. Elwany, Uncertainty propagation analysis of computational models in laser powder bed fusion additive manufacturing using polynomial chaos expansions, J. Manuf. Sci. Eng. 140 (12).
[44] M.C. Kennedy, A. O'Hagan, Bayesian calibration of computer models, J. R. Stat. Soc. Ser. B (Stat. Methodol.) 63 (3) (2001) 425–464.
[45] G. Tapia, L. Johnson, B. Franco, K. Karayagiz, J. Ma, R. Arroyave, I. Karaman, A. Elwany, Bayesian calibration and uncertainty quantification for a physics-based precipitation model of nickel-titanium shape-memory alloys, J. Manuf. Sci. Eng. 139 (7).
[46] Z. Wang, P. Liu, Y. Ji, S. Mahadevan, M.F. Horstemeyer, Z. Hu, L. Chen, L.-Q. Chen, Uncertainty quantification in metallic additive manufacturing through physics-informed data-driven modeling, JOM 71 (8) (2019) 2625–2634.
[47] M. Mahmoudi, G. Tapia, K. Karayagiz, B. Franco, J. Ma, R. Arroyave, I. Karaman, A. Elwany, Multivariate calibration and experimental validation of a 3D finite element thermal model for laser powder bed fusion metal additive manufacturing, Integ. Mater. Manuf. Innov. 7 (3) (2018) 116–135.
[48] M. Mahmoudi, Process monitoring and uncertainty quantification for laser powder bed fusion additive manufacturing, Ph.D. thesis, Texas A&M University (2019).
[49] See supplementary material.
[50] C. Montgomery, J. Beuth, L. Sheridan, N. Klingbeil, Process mapping of inconel 625 in laser powder bed additive manufacturing, Solid Free. Fabr. Symp. (2015) 1195–1204.
[51] L. Scime, J. Beuth, Using machine learning to identify in-situ melt pool signatures indicative of flaw formation in a laser powder bed fusion additive manufacturing process, Addit. Manuf. 25 (2019) 151–165.
[52] W.E. King, H.D. Barth, V.M. Castillo, G.F. Gallegos, J.W. Gibbs, D.E. Hahn, C. Kamath, A.M. Rubenchik, Observation of keyhole-mode laser melting in laser powder-bed fusion additive manufacturing, J. Mater. Process. Technol. 214 (12) (2014) 2915–2925.
[53] G.G. Gladush, I. Smurov, Physics Of Laser Materials Processing: Theory And Experiment, Springer Science & Business Media, 2011.